Abstract

ELKINS, JASON ROBERT. Efficient Uncertainty Quantification for a Fast-Spectrum Generation IV Reactor System. (Under the direction of Hany S. Abdel-Khalik.)

This research is part of on-going research on the management of uncertainties in simulator predictions for Generation IV systems via optimum experimental design. The focus is on uncertainties originating due to input data. The objective is to devise an algorithmic framework for quantification of uncertainties, identification of their key sources, and ultimately guiding the design of validating experiments for their reduction. An integral part of this research is the development of uncertainty quantification algorithms for models involving many input data and output responses. This represents the focus of the research reported here.

Uncertainty Quantification (UQ) in nuclear systems simulation is playing an increasing role in supporting decisions related to the research and development of advanced nuclear energy systems, especially those of interest to the Global Nuclear Energy Partnership (GNEP) and Next Generation Nuclear Plant (NGNP) programs. UQ will help assess the adequacy of existing simulation tools and associated databases, e.g. nuclear cross-section data, and provide guidance to areas of models and/or data where further development and/or measurements should be prioritized. A sensitivity and uncertainty analysis has been conducted to study the effects of neutron microscopic cross-section data uncertainty on macroscopic attributes that influence reactor core design, performance and safety for a Generation IV reactor concept. In the realm of reactor engineering, neutron cross-section data represents the basic physics of neutron interactions with matter and therefore have large impacts on evolution of flux, power,

reactivity and other reactor performance attributes. Currently, we focus on uncertainties originating from cross-section data uncertainties, believed to be of primary significance for fast reactor calculations.

This thesis presents a recent development of an UQ algorithm for increasing the efficiency of UQ to a level that enables its execution on a routine basis with best estimate calculations for various reactor performance attributes. Our objective is to devise an algorithm that can characterize uncertainties in the multitudes of reactor performance attributes as evaluated by reactor simulation tools on a routine basis with reference calculations.

The results of this study includes an efficient UQ analysis of calculated uncertainties for chosen key core attributes believed to greatly affect reactor core performance and safety, and an identification of key neutron cross-sections that contribute the most to important core attributes uncertainties.

Efficient Uncertainty Quantification for a Fast-Spectrum Generation IV Reactor System

by
Jason R. Elkins

A thesis submitted to the Graduate Faculty of
North Carolina State University
in partial fulfillment of the
requirements for the Degree of
Master of Science

Nuclear Engineering

Raleigh, North Carolina

2008

APPROVED BY:

Dr. Paul J. Turinsky Co-Chair	Dr. Agnes Szanto Committee Member

Dr. Hany S. Abdel-Khalik
Chair of Advisory Committee

Dedication

To Grandma.

Biography

Jason Robert Elkins was born in Greensboro, North Carolina at Moses Cone Hospital on April 26, 1984 to John and Judy Elkins. He received his elementary and secondary education from Liberty Elementary and Middle School located in Liberty, North Carolina. He later attended Eastern Randolph High School of Ramseur, North Carolina and graduated 4th out of 207 students in 2002.

After his high school education, Jason was accepted into the College of Engineering at North Carolina State University of Raleigh, North Carolina. After enrolling into the Department of Nuclear Engineering, his summers consisted of internships at Knolls Atomic Power Laboratory of Schenectady, New York and Duke Energy of Charlotte, North Carolina. He received his Bachelor's of Science in May 2006 from the Department of Nuclear Engineering, graduating Summa Cum Laude. Following graduation, Jason began work toward a Master's of Science in Nuclear Engineering under the direction of Dr. Hany S. Abdel-Khalik.

Jason has accepted a position at Duke Energy at the General Office location in Charlotte, North Carolina and will begin work upon completion of his Master's degree.

Acknowledgments

Throughout my academic career, I have had an immense amount of support from so many people so please forgive me if I leave someone out. First I want to recognize and thank my parents, John and Judy Elkins, for always providing me with more than enough support to reach all of my goals. During my hardest times at school, I could always count on visiting them for comfort. I would also like to thank my brother, Bret Elkins, for being the most wonderful brother and friend that I could ask for. Finally, I want to thank the soon-to-be Mrs. Elkins, Alex Lucas, for always being there no matter what. It was because of you that I was able to make it through the worst of times and you who created the best.

I offer sincere gratitude to my advisor Dr. Hany Abdel-Khalik for his excellent guidance and knowledge that he shared with me while I was in graduate school. I truly thank you for treating me as an equal as we worked together and for putting up with all of my questions that I would bring to you time and time again. Next, I thank Dr. Paul Turinsky who has been continuously available to answer any questions that I had. I would also like to thank my friends and classmates who have provided support and help with my work. Particularly, I would like to thank Mr. Tracy Stover for sharing his vast knowledge on uncertainty propagation techniques along with his help pertaining to the REBUS model. Further, I would like to thank Mr. Ross Hays, Mr. Matt Jessee and Mr. Christopher Briggs for providing programming knowledge. Finally I would like to thank Mr. Tyler Schweitzer for being such a great friend these past five and half years of undergraduate and graduate school.

Table of Contents

List of Figures

List of Tables

Nomenclature

Acronyms:

ABTR	**A**dvanced **B**urner **T**est **R**eactor
BOC	**B**eginning **O**f **C**ycle
DC	**D**esign Basis **C**ore Simulator
DOF	**D**egrees **O**f **F**reedom
EFPD	**E**ffective **F**ull **P**ower **D**ay
ENDF	**E**valuated **N**uclear **D**ata **F**ile
EOC	**E**nd **O**f **C**ycle
ESM	**E**fficient **S**ubspace **M**ethods
HFP	**H**ot **F**ull **P**ower
HM	**H**eavy **M**etal
I/O	Input/Output Data Stream
LWR	**L**ight **W**ater **R**eactor
LWR-SF	**L**ight **W**ater **R**eactor-**S**pent **F**uel
MT	**M**etric-**T**onnes
MWD	**M**ega-**W**att-**D**ay
PDF	**P**robability **D**ensity **F**unction
RMS	**R**oot **M**ean **S**quare
SVD	**S**ingular **V**alue **D**ecomposition
TRU	**T**ransuranic(s)
UQ	**U**ncertainty **Q**uantification
WG-Pu	**W**eapons-**G**rade **P**lutonium

ZPPR	**Z**ero **P**ower **P**hysics **R**eactor

1 Introduction

1.1 Purpose

Since the emergence of nuclear power generation, designers have worked to build nuclear reactors that are safe, reliable and efficient. Today, research and development is highly focused on areas pertinent to advanced reactor design systems. The U.S. Department of Energy has created many programs that fall into this category, such as the Advanced Fuel Cycle Initiative (AFCI), the Global Nuclear Energy Partnership (GNEP), Next Generation Nuclear Plant (NGNP) and Advanced Energy Initiative (AEI). This thesis is supported by an on-going research program that focuses on understanding and managing the prediction uncertainties that originate from the uncertainties of physical data that are used in simulation and modeling tools for a Generation IV reactor concept. The goals of this study are to a) quantify the uncertainties for specific reactor core attributes that greatly affect core performance and safety, and b) determine which physical data contribute the most to reactor core attribute uncertainties. With these core attributes uncertainties understood, optimization upon current design margins could be utilized. Additionally, reactor designers would have the opportunity to evaluate the cost-benefit of reducing these uncertainties by experimentation and/or improving the accuracy of modeling systems. Finally, the core attribute uncertainties calculated in this research will build a framework for other studies to follow. One parallel study will be to design an experiment utilizing Argonne National Laboratories (ANL) Zero Power Physics Reactor (ZPPR) that harnesses the quantified uncertainties calculated in this thesis to further reduce model data uncertainties where determined appropriate. The focus of this study

will be confined to the development and utilization of an UQ algorithm in support of the research goals listed above.

1.2 Core Simulator Background

The operation of advanced nuclear reactors will place more stringent requirements on the acceptable accuracy of core simulation tools used in support of design and operation. Core simulators enable designers to model reactor operation, performance, and safety before the expensive construction of the plant takes place. Quantification and understanding of simulators' uncertainties also allow designers the freedom to change design to reduce design margins which greatly affect operational cost and profit. In addition, with the introduction of advanced reactor systems, i.e. Generation IV reactor systems, the accuracy of the simulation tools needs to be assessed in regard to key core attributes such as decay heat, peak fast fluence, discharge burnup, coolant void worth, etc since the experience with light water reactors (LWR) will not provide an informed basis for assessment due to the large difference in irradiation environment. It is the purpose of this study to use the method of uncertainty quantification to calculate uncertainties found in key core attributes for an advanced reactor system due to cross-sections uncertainties.

1.3 Uncertainty Quantification

Uncertainty quantification (UQ) in nuclear systems simulation is playing an increasing role in supporting decisions related to the research and development of advanced nuclear energy systems. UQ will aid in the understanding of the key core attributes uncertainties that are associated with these advanced reactor systems. Such uncertainties arise from simulator input database uncertainties, e.g. cross-section data errors, numerical discretization errors and modeling approximations. Few-group cross-

section data represents the bulk of input data to core simulation tools, and will be the focus of this UQ study. UQ of key core attributes will provide guidance to models and/or data where further development and/or measurements should be prioritized to reduce attributes uncertainties. Sensitivity and uncertainty analysis of calculated uncertainty estimates is vital in safety analysis, since the reliability of the predictions must be known in order to set realistic design margins for reactor systems; and further reduces the reliance on over-conservatism in design. The target is that by identifying key uncertain cross-sections to which the response is most sensitive, one will be able to improve the cross-sections database used in the analysis and thereby improve the accuracy of the calculations [15].

This thesis presents a recent development of an UQ algorithm for increasing the efficiency of UQ to a level that enables its execution on a routine basis with best estimate calculations for various reactor performance attributes, which denote important reactor core responses. The objective is to devise an algorithm that can characterize uncertainties in the multitudes of reactor performance attributes as evaluated by reactor simulation tools. Some of these attributes include the three-dimensional power and fluence distributions, reactivity coefficients, thermal limits and possible in-core instrumentation readings. Currently, the focus is based on uncertainties originating from cross-section data uncertainties, believed to be of primary significance to fast reactor calculations. To achieve this goal, one must overcome the computational challenges posed by the complexity of reactor simulation tools and their associated large input and output (I/O) data streams. Calculated uncertainties translate into cost of margin which is required to ensure safe and reliable operation of the reactor.

Our proposed approach reduces the number of model evaluations via the utilization of the Efficient Subspace Methods (ESMs) [3]. ESM is primarily used to perform uncertainty and sensitivity analysis for applications that contain large (I/O) data streams while minimizing the number of required model evaluations. The use of the ESM method has been proven very useful in thermal reactor UQ calculations and has shown that cross-sections uncertainties present a major source of error in thermal reactor calculations [4]. This thesis extends the applicability of ESM to advanced reactor design concepts, specifically sodium cooled fast reactors.

1.4 Uncertainty Quantification Techniques

There are many different types of data originated UQ techniques that have been developed over the years, and a few key techniques are noted below. These techniques include a deterministic and stochastic forward model approach, an adjoint model approach, and a subspace approach which was ultimately used for this study. However, performing uncertainty calculations can be challenging due to large input/output data streams that are associated with reactor system modeling tools. Uncertainties also arise from numerical discretization approximations and homogenization theory modeling approximations along with finite arithmetic round-off error. For this study, numerical and modeling errors will be neglected and only uncertainties due to cross-sections will be investigated.

1.4.1 Deterministic Forward Technique

Fundamentally, there are two deterministic UQ methods that can be used for uncertainty quantification, e.g. the forward and adjoint perturbation methods. The most basic uncertainty technique, which is through a forward approach, is performed by

varying selected input data one at a time in order to observe an output response. By observing how the output changes via input data perturbation, sensitivity information can be drawn about the perturbed input data. Repeating this methodology over a range of input parameters constructs a sensitivity operator which is used in many sensitivity and uncertainty analyses. This method can be used to propagate uncertainties in models' input data [14]. Let the matrix $\mathbf{C}$ denote an input data covariance-variance matrix. Additionally, let us denote $\mathbf{R}$ as a response and $\mathbf{S}$ a sensitivity operator where the i^{th} element of $\mathbf{S}$ is defined by:

$$[\mathbf{S}_i] = \frac{\partial \mathbf{R}}{\partial \alpha_i}. \tag{1.4-1}$$

Eq. (1.4-1) shows that the sensitivity operator is merely the change in response to some input parameter, α_i. One can show that the response uncertainty, in units of variance, is given by:

$$\text{var}(\mathbf{R}) = \mathbf{SCS}^{\mathbf{T}}, \tag{1.4-2}$$

where the variance of the response is calculated by "sandwiching" the input data covariance matrix between the conformable forms of the sensitivity operator – this relation is often called 'the sandwich equation'. Even though this method works, calculating the sensitivity matrix and performing the mathematical operation shown in Eq. (1.4-2) is very time consuming and will not be feasible with models that have large amounts of input data.

1.4.2 Adjoint Technique

Another method for sensitivity analysis is based on the calculation of the adjoint solution which can be considered as a reverse approach to the forward-model. The

highlight of the adjoint methodology is that sensitivity coefficients can be calculated for a particular response due to all input data. An ideal setting for this method occurs when there are comparatively fewer responses, m, than input parameters, n, i.e. where $m < n$. Typically, sensitivity coefficients are calculated for selected core responses, thus a sensitivity matrix for each response pertaining to all input data can be created. As seen in the work by G. Aliberti, et al., a core attribute covariance matrix can be determined by multiplying the sensitivity matrix by the input data covariance matrix, and finally by the transposed sensitivity matrix [11]. Additionally, the adjoint method in Aliberti's study was used to calculate uncertainties in reactor and fuel cycle parameters in regard to cross-section perturbation [11],[13]. However, sensitivity analysis by adjoint methodology can become time consuming when the number of responses is large, which occurs often in reactor calculations.

1.4.3 Stochastic Forward Technique

Another forward technique is known as stochastic sensitivity analysis. This approach works for systems that have larger input and output data streams [14], which is more appropriate for this study. Further, this method uses Monte Carlo sampling techniques, which can be random, orthogonal, or Latin hypercube in which all assume some input data statistical distribution [16]. In a brief description, random sampling selects points without taking into account points that have been chosen previously. Orthogonal sampling divides the entire space of samples into equal subspaces while simultaneous sampling creates a total ensemble of points like a Latin hypercube sample; Latin hypercube sampling demands for a prescribed number of sampled points that are divided so that the range of each variable is divided into equal probability intervals [16].

Observing the output after running such input data through computational models allows one to check the distribution in post processing analysis. A great benefit of Monte Carlo sampling is its randomness, which creates an unbiased approach in regards to data sampling. In other words, all data that exists within the input data space has an equal opportunity of being sampled, whereas a biased approach would disregard certain data to help shape output quantities in a particular fashion.

1.4.4 Subspace Technique

ESM is primarily used to perform S/U analysis for applications that contain large (I/O) data streams while minimizing the number of required model evaluations. Such an application is Multi-Scale/Multi-Physics (MSMP) modeling. "Recently, MSMP modeling has proven to be essential to the successful modeling of the full fuel cycle where a wide spectrum of physical processes occur with large variations in time and spatial scales such as neutron physics, heat transfer, partitioning and reprocessing, and waste management, etc" [3][17][1]. For an ill-conditioned problem, ESM approximates the behavior of large rank deficient matrices such as the sensitivity and covariance matrices in an efficient form. As shown in Eq. (1.4-2), the variance of response parameters can be determined via the sandwich equation; however, obtaining the sensitivity operator along with calculating this product can become very time consuming. ESM utilizes the fact that there normally exists a dimensionality reduction in this calculation thus reducing the number of model evaluations necessary for this calculation. Therefore, a substantial reduction in computational run-time can be achieved.

[1] Quotations denote direct referencing.

1.5 Computational Modeling Description

Reactor system modeling is a tool that is utilized in all segments of the nuclear industry for reactor design, optimization and safety. These models map neutronic interaction with various isotopes to simulate core power, flux spectra, depletion characteristics, etc. Generally, a many-group cross-section library that exists for all isotopes in the model must be utilized. For computational storage and run-time efficiencies, these many-group cross-section libraries are collapsed to few-group cross-section libraries via a processor that performs a lattice physics or pin-cell calculation using flux-averaging and resonance treatment techniques. A core simulator model utilizes the few-group cross-section library and calculates many core attributes.

For this UQ application, which focuses on an advanced reactor system, a cross-section library processor (MC^2-2) was used to collapse a many-group cross-section library (ENDF) and a fast reactor simulator (REBUS-3) was utilized to model the core. A black box flow diagram of this modeling process is shown in Figure 1.

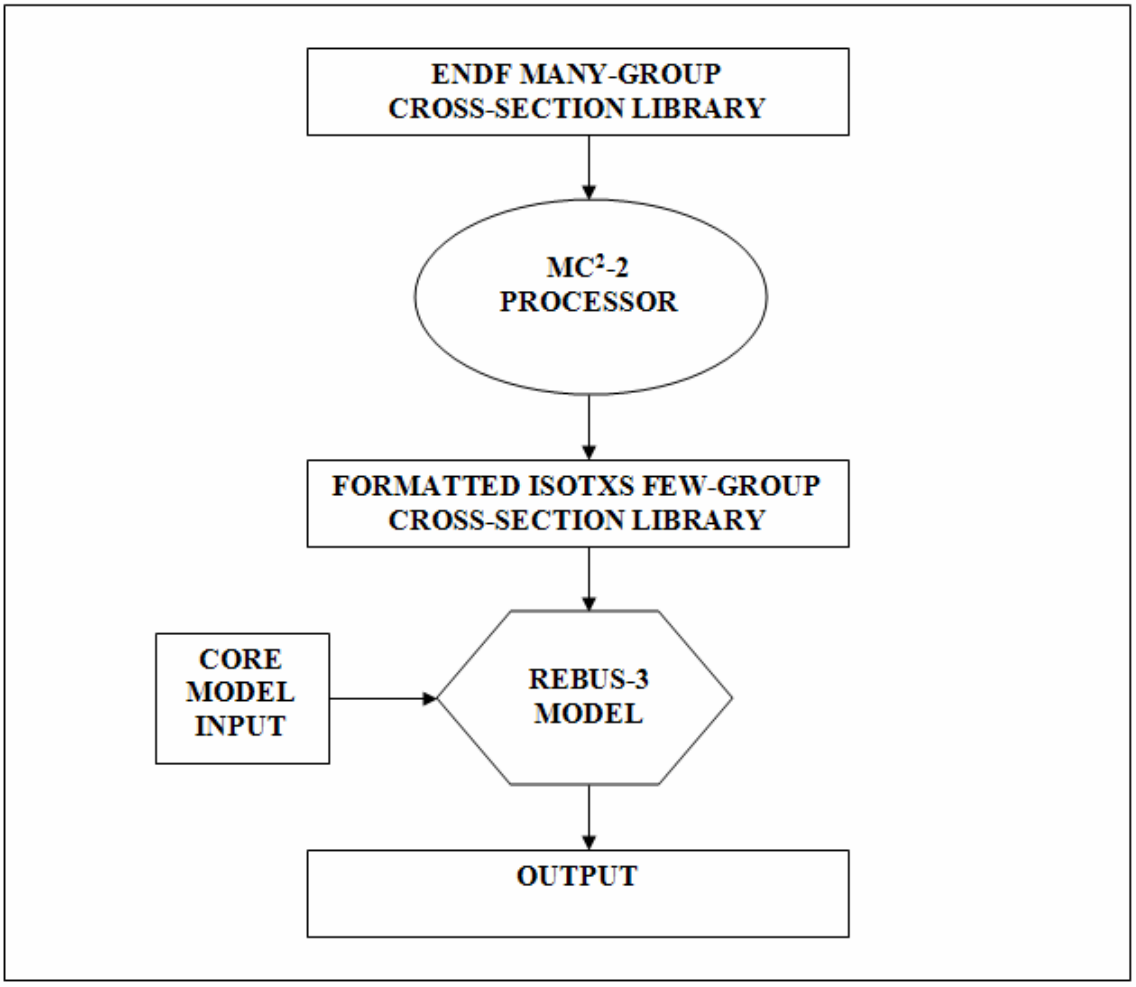

Figure 1: Black Box Modeling Flow Diagram

Section 1.5.1 and section 1.5.2 describe in detail the MC^2-2 processor and REBUS-3 model used in this study, respectively.

1.5.1 MC^2-2 Description

MC^2-2 is a processor used for calculating fast neutron spectra and multi-group cross-sections from ENDF/B data libraries. This code was created by Argonne National Laboratory (ANL) and distributed by the Radiation Safety Information Computational Center (RSICC) located in Oak Ridge National Laboratory (ORNL). MC^2-2 solves the neutron slowing-down equations using basic neutron data from the ENDF/B-V data files.

The spectrum that is calculated by MC^2-2 is used to collapse multi-group to few-group neutron cross-section data. Eq. (1.5-1) presents the general formulation used to calculate macroscopic few-group cross-sections via flux weighting techniques.

$$\bar{\Sigma}_{x_g} = \frac{\int_{E_g}^{E_{g-1}} dE \Sigma_x(E)\phi(E)}{\int_{E_g}^{E_{g-1}} dE \phi(E)} \tag{1.5-1}$$

where $\bar{\Sigma}_x$ is the effective macroscopic cross-section over selected energy groups, $E_g < E < E_{g-1}$, which is weighted by the group dependent neutron flux. MC^2-2 accommodates high-order P scattering representations and provides numerous capabilities such as delayed neutron processing, isotope mixing, free-format input, and flexibility in output data selection. A fundamental mode homogeneous unit cell calculation is performed using a multi-group or a continuous slowing-down treatment. Multi-group neutron homogeneous cross-sections are then finally generated into an ISOTXS format for an arbitrary group structure [5].

1.5.2 REBUS-3 Description

REBUS-3, here forth denoted as REBUS, is a code system that is designed for the analysis of fast reactor fuel cycles. Much like MC^2-2, REBUS was created by ANL and distributed by the RSICC which is located at ORNL. "Two basic types of analysis problems are solved: 1) the infinite-time, or equilibrium, conditions of a reactor operating under a fixed fuel management scheme, or 2) the explicit cycle-by-cycle, or non-equilibrium operation of a reactor under a specified periodic or non-periodic fuel management program" [10]. The code models fuel depletion over a user-specified cycle

length and fuel management scheme. REBUS is also a deterministic core model. Finally REBUS is equipped to model hexagonal-z geometry fuel assembly arrays, which is the design for this study.

Additionally, a 15-group MC^2-2 -- REBUS model was used as the basis for this study [20].

2 ABTR Description

An Advanced Burner Test Reactor (ABTR) was chosen for this study, which is based on a General Electric Hitachi Nuclear's S-PRISM (SuperPRISM) Fast Reactor Design. S-PRISM is a pool-type, modular design for a sodium-cooled fast reactor designed to operate near breakeven or as a breeder reactor [1]. The ABTR core model is a 250MWt/96MWe liquid sodium-cooled fast reactor that consists of 199 hexagonally shaped assemblies. A breakdown of these assemblies are as follows: 54 driver assemblies, 78 reflector assemblies, 48 shield assemblies, 10 control rod assemblies and 9 test assemblies, where 6 of these test assemblies are referred as middle-core assemblies in this thesis. The 54 driver assemblies are divided into two enrichment zones, denoted as an inner and outer core region; 24 inner-core fuel assemblies with a TRU fuel enrichment of 16.5% and 30 outer-core fuel assemblies with a TRU fuel enrichment of 20.7%. A ternary metal alloy fuel for the 54 driver assemblies was chosen to be (U-TRU-10Zr) with a 94.2% fissile content WG-Pu feed. The 6 test assemblies, or middle-core assemblies, are identical to the driver assemblies except that LWR-SF TRU fuel is used. Table 1 presents the TRU isotopic composition for the weapons grade plutonium and LWR-SR TRU driver fuels.

Table 1: TRU Isotopic Composition (%)

	WG-Pu	LWR-SF TRU
Np-237	0.00	4.60
Pu-238	0.01	1.35
Pu-239	93.81	51.77
Pu-240	5.81	23.67
Pu-241	0.35	7.80
Pu-242	0.02	4.67
Am-241	0.00	5.08
Am-242m	0.00	0.01
Am-243	0.00	0.88
Cm-243	0.00	0.00
Cm-244	0.00	0.17
Cm-245	0.00	0.01
Cm-246	0.00	0.00

Each reflector assembly is composed of 91 HT-9, 'high temperature', solid pins which are arranged in a triangular pitch array. The shielding assemblies contain 19 pins which are composed of HT-9 cladding along with a natural boron and B_4C combination.

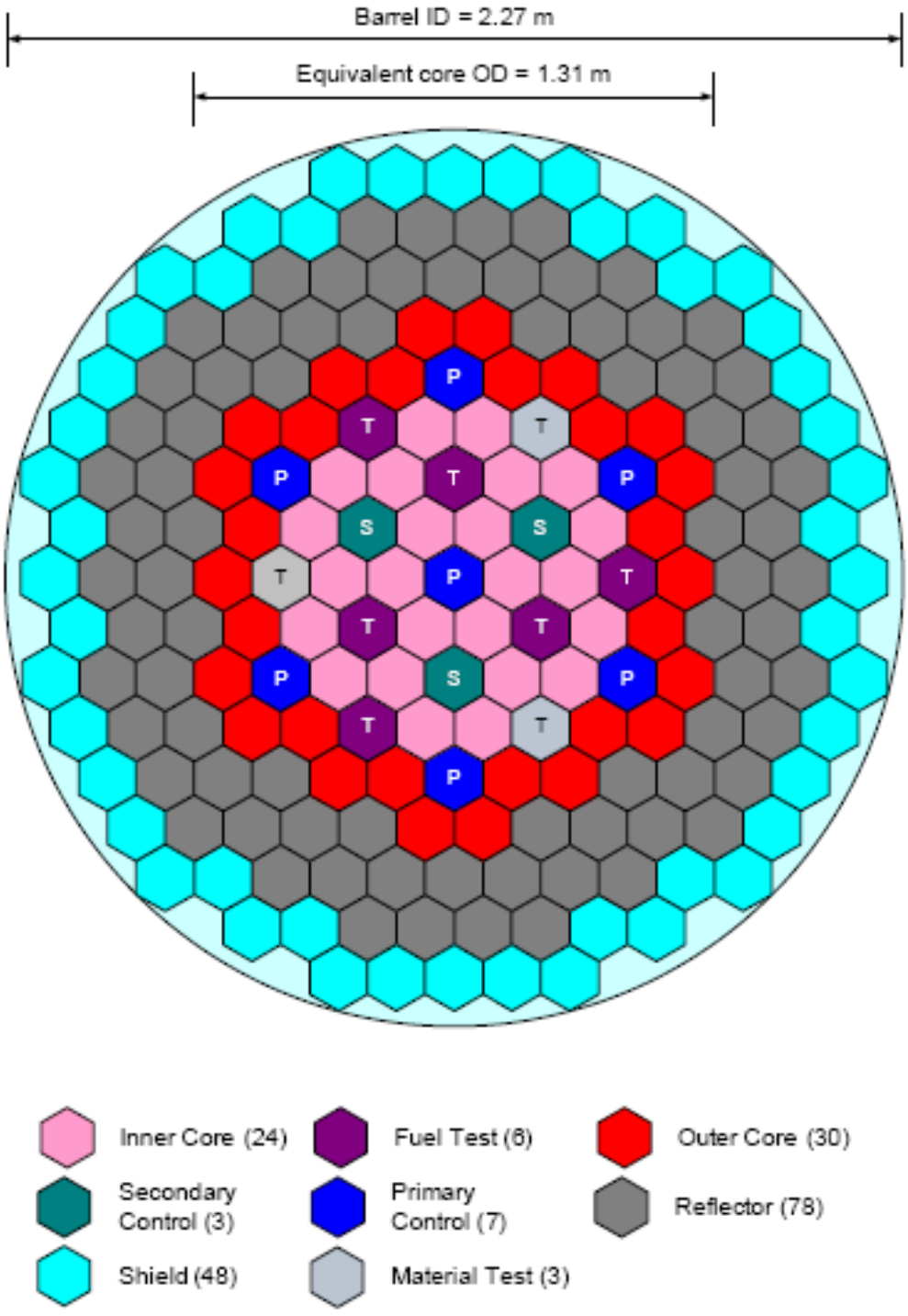

Figure 2: ABTR Core Configuration

Figure 2 provides a geometrical layout for the 199 assemblies present in this fast reactor design.

Table 2 shows the inventory makeup along with mass flow rates for the U-TRU-Zr fuel.

Table 2: (U-TRU-Zr) HM/TRU Inventory and Mass Flow Rate

	Inventory, kg		Mass flow, kg/year	
Isotope	BOEC	EOEC	charge	discharge
U-234	0.0	0.0	0.00	0.01
U-235	5.2	5.0	1.52	0.84
U-236	0.3	0.4	0.00	0.14
U-238	3289.6	3270.2	768.35	710.29
Np-237	3.6	3.6	0.89	0.88
Pu-236	0.0	0.0	0.00	0.00
Pu-238	1.6	1.7	0.28	0.56
Pu-239	628.6	617.0	156.83	121.80
Pu-240	80.2	83.1	13.74	22.29
Pu-241	8.9	9.0	2.09	2.26
Pu-242	4.0	4.0	0.96	1.03
Am-241	3.8	3.8	1.00	0.90
Am-242	0.1	0.1	0.00	0.05
Am-243	0.7	0.8	0.18	0.20
Cm-242	0.1	0.1	0.00	0.04
Cm-243	0.0	0.0	0.00	0.00
Cm-244	0.2	0.2	0.03	0.06
Cm-245	0.0	0.0	0.00	0.01
Cm-246	0.0	0.0	0.00	0.00
Total heavy metal	4027.2	3999.0	945.9	861.3
Total TRU	732.0	723.4	176.0	150.1

In Table 2, U^{238} and Pu^{239} are the key isotopes that contribute the highest inventory for this core design. U^{238} contributes 81.68% of HM inventory while Pu^{239} makes up 85.87% of TRU loading. Pu^{239} is created via a neutron capture reaction with U^{238}, which creates U^{239} and further decays into Np^{239} and finally Pu^{239}. Per cycle, two inner and two outer fuel drivers are required and Table 2 verifies that U^{238} and Pu^{239} are charged and discharged from the core at much higher mass flow rate in comparison to other HM isotopes.

The ABTR operates in four-month cycles and has an average/peak discharge

burnup of 97.7/130.8 MWd/kg and a fissile/TRU conversion ratio of 0.58/0.65. Reactivity control and neutronic shutdown are provided from the use of 7 primary and 3 secondary control assemblies via bank movement mechanisms. The shutdown margin for the primary system, assuming that the most reactive assembly is stuck out, is 7.63$ at BOEC and 12.88$ at EOEC [2].

The primary cooling system consists of a pool-type arrangement of liquid sodium that is connected to an intermediate sodium loop. A supercritical CO_2 Brayton Cycle power generation cycle was proposed for this study. A plot of the overall thermodynamic cycle for this proposed ABTR design can be seen in Figure 3.

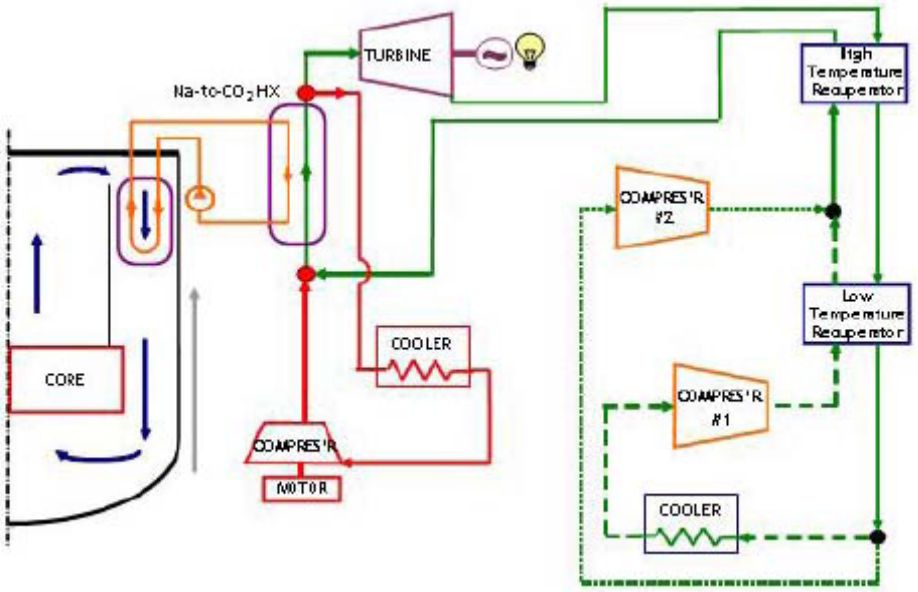

Figure 3: ABTR Thermodynamic Cycle

As seen in Figure 3, the intermediate sodium loop connects to the supercritical CO_2 Brayton Cycle by the means of a Na-to-CO_2 heat exchanger where heated CO_2 flows into a turbine generator [2]. The superheated gas propels turbine blades, which generates electricity for the grid.

3 Methodology

The proposed approach is based on the use of the Efficient Subspace Method (ESM), which derives its power from the following three assumptions: A) local linearity of the computational model within range of input data uncertainties, B) ill-conditioning of the covariance matrix characterizing input data uncertainty information, and C) ill-conditioning of the model sensitivity matrix. If condition A is not satisfied, the estimated uncertainties will be only first-order accurate. Conditions B and C are not necessary; however, they correlate the UQ-associated calculational overhead to the degree of ill-conditioning of the input data covariance and model sensitivity matrices.

3.1 Model Local Linearity

Model local linearity is an important aspect that must be taken into account so that key core attribute uncertainties are calculated correctly and that the ESM method can be utilized. As mentioned previously, a fast reactor fuel cycle model (REBUS) was selected to model the ABTR core for a converted equilibrium to non-equilibrium scenario (will be discussed in a later section). REBUS is a non-linear model; however, with the use of local linearity by remaining in range of input data uncertainties, key core response (i.e. attribute) uncertainties can be calculated.

A model $\vec{\Omega}$ that maps $\vec{\sigma} \in \Re^n$ to $\vec{y} \in \Re^m$ can be approximated by a local linear function around a reference point $(\vec{\sigma}_0, \vec{y}_0)$ if it satisfies the following condition:

$$\vec{\Omega}(\vec{\sigma}') - \vec{\Omega}(\vec{\sigma}_o) = \sum_{i=1}^{k} \alpha_i \left[\vec{\Omega}(\vec{\sigma}_i) - \vec{\Omega}(\vec{\sigma}_o) \right] \qquad (3.1\text{-}1)$$

where $\bar{\sigma}$ and $\bar{y}$ are vectors characterizing n input data and m performance attributes, respectively. For the remainder of the paper, we identify variables with single bars as vectors and bold font as matrices. The vector $\bar{\sigma}_i = \bar{\sigma}_o + \delta\bar{\sigma}_i$ describes the input data after being perturbed from their reference values by k random perturbation $\{\delta\bar{\sigma}_i\}$. Each perturbation $\delta\bar{\sigma}_i$ is selected to be linearly independent from all other $k-1$ perturbations. The $\bar{\sigma}'$ is a vector of input data perturbed by a linear combination of the previously selected k random perturbations, i.e.

$$\bar{\sigma}' = \bar{\sigma}_o + \sum_{i=1}^{k} \alpha_i \delta\bar{\sigma}_i \tag{3.1-2}$$

Satisfaction of Eq. (3.1-2) assures linearity of the performance attributes changes with respect to all input data. If some performance attribute exhibits a non-linear relationship with respect to some input data, Eq. (3.1-1) will not be satisfied. The residual of Eq. (3.1-1) can measure the deviation from linear behavior, here denoted by the non-linear error.

This study serves to identify two limits on the sizes $\{\alpha_i\}$ of input data perturbations: a) an upper limit γ^U is selected high enough to ensure that the perturbations cover the ranges of input data uncertainties (i.e. within 4 standard deviations of their respective mean values). This is important to ensure that the computational model behaves linearly with input data varying at the tail ends of their distributions. And b) a lower limit γ^L is selected to determine the minimum size of input data perturbations that can induce noticeable changes in performance attributes. These upper and lower cross-section perturbation limits will be found via a prescribed

numerical tolerance limit, ζ , that is subject to engineering judgment and is determined by the analyst.

To determine the upper limit γ^U and lower limit γ^L for input data perturbation sizes, two linearity tests were employed. Along with these limits, the linearity tests aid in finding the local linearity region in REBUS for perturbing the input data. There were two techniques used to determine the range, or standard deviation in this case, at which cross-sections could be perturbed and REBUS would remain in a linear region.

3.1.1 Scaled Random Cross-Section Perturbation Study

The first technique was to create one random direction, where a direction refers to a certain perturbation of input cross-section data from a reference condition. Randomness of each cross-section perturbation is important to ensure that all cross-sections will be perturbed without a biased approach. The size of the cross-sections perturbations would then be scaled, using some scaling factor, in that same random direction. Linearity confirms that scaling the input will produce an output perturbation proportional to the size of the scaling factor. By using different scaling factors, the linearity range for REBUS can be found. This linearity method was used to calculate the upper limit, γ^U for cross-section perturbation, after exploring several random directions and repeating the scaling procedure described above. The implication is that if the cross-sections perturbations exceed the upper limit γ^U then REBUS will behave non-linearly. Based on a prescribed numerical tolerance limit, ζ , which varies based upon the reactor system attribute, a maximum cross-section perturbation was found. This follows when:

$$\left|\left(\bar{\Omega}\left(\vec{\sigma}_o+\alpha\delta\vec{\sigma}_i\right)-\bar{\Omega}\left(\vec{\sigma}_o\right)\right)-\alpha\left(\bar{\Omega}\left(\vec{\sigma}_o+\delta\vec{\sigma}_i\right)-\bar{\Omega}\left(\vec{\sigma}_o\right)\right)\right|>\zeta \qquad (3.1\text{-}3)$$

where ζ is a prescribed tolerance limit, α denotes the scaled standard deviation, σ_i is the ith perturbed cross-section and σ_o is the reference cross-section. By scaling the cross-section perturbation vector, one can find when the left-hand side (LHS) of Eq. (3.1-3) becomes greater than the numerical tolerance limit. At this point, the non-linear error exceeds the tolerance limit and thus the upper numerical limit, γ^U, for perturbing cross-sections is found, where $\gamma^U = \alpha$.

Furthermore, the numerical tolerance limit was also used to calculate the lower limit γ^L, or minimum perturbation for cross-section data that would still produce some noticeable change in modeled output that exist above the non-linear error margin. Similar to finding the upper limit, γ^U, calculating the lower limit revolved around some prescribed numerical tolerance limit, denoted as ζ. Depending on the attribute, this tolerance limit was based on engineering judgment along with knowledge from thermal reactor analysis [4]. Accordingly, for some random cross-section perturbation direction, a minimum scaling factor was found such that the absolute change in an attribute from running the perturbed and unperturbed cross-sections became less than the numerical tolerance limit, i.e.,

$$\left|\vec{\Omega}\left(\vec{\sigma}_o + \alpha\delta\vec{\sigma}_i\right) - \vec{\Omega}\left(\vec{\sigma}_o\right)\right| < \zeta . \qquad (3.1\text{-}4)$$

As α is decreased, the difference in attributes calculated from the perturbed and unperturbed cross-section inputs will also decrease. The point at which the LHS of Eq. (3.1-4) becomes less than the tolerance limit is when the lower limit for cross-section perturbation will emerge, i.e. $\gamma^L = \alpha$. By setting a lower limit for cross-section

perturbation, responses will behave linearly due to this cutoff from non-linear error.

3.1.2 Multiple Random Cross-Section Perturbation Study

Although the previous linearity test allowed for the calculation of the upper and lower standard deviation limits, the second test served as a 'sanity check' to evaluate the model at these standard deviations where $\sigma \in \left[\gamma^L, \gamma^U\right]$. This technique was to allow a random number generator to produce random directions. This linearity test differs from the former because this test observes the linearity of *n* primary directions rather than one. Linearity also shows that if there are *n* random directions, then a linearly combined case, which is the summation of each random direction multiplied by a random scaling factor can be approximated using a linear model. For this study, it is imperative that the square of scaling factors sum to 1 to ensure that the linearly combined cross-section vector will have the same size as individual cross-section vectors. In equation form, let $\left[\vec{\sigma}_1,\ \vec{\sigma}_2,\ \ldots,\ \vec{\sigma}_n\right]$ denote random cross-section vectors which span from $i = 1 \ldots n$. The linearly combined cross-section vector is defined below in Eq. (3.1-5),

$$\vec{\sigma}_{LC} = \vec{\sigma}_o + \sum_{i=1}^{n} \alpha_i \delta\vec{\sigma}_i \tag{3.1-5}$$

where,

$$RMS\left(\vec{\sigma}_i\right) = \sqrt{\frac{\sum \vec{\sigma}_{i,j}{}^2}{n}} = \sigma_{\vec{\sigma}_i}. \tag{3.1-6}$$

The root mean square (RMS), or quadratic mean, for each individual cross-section vector was set so that $\sigma_{\vec{\sigma}} \in \left[\gamma^L, \gamma^U\right]$, which was set to a conservative 5% in the study.

Following methodology by Waller [21], let us derive the standard deviation of the

linearly combined cross-section vector, $\vec{\sigma}_{LC}$. First, let us introduce the expected value and variance for a given cross-section vector as $E(\vec{\sigma}_i) = \vec{\mu}_i$ and $V(\vec{\sigma}_i) = \sigma^2_{\vec{\sigma}_i}$, respectively. Taking the first moment or expected value of $\vec{\sigma}_{LC}$ yields:

$$E(\vec{\sigma}_{LC}) = \vec{\mu}_{\vec{\sigma}_{LC}} = \vec{\sigma}_o + \sum_{i=1}^{n} \alpha_i \vec{\mu}_i \tag{3.1-7}$$

where the expected value of the reference cross-section vector returns itself. Now take the second moment of the variance of $\vec{\sigma}_{LC}$:

$$\sigma^2_{\vec{\sigma}_{LC}} = E\left(\vec{\sigma}_{LC} - \vec{\mu}_{\vec{\sigma}_{LC}}\right)^2 \tag{3.1-8}$$

where

$$\vec{\sigma}_{LC} - \vec{\mu}_{\vec{\sigma}_{LC}} = \left(\vec{\sigma}_o + \sum_{i=1}^{n} \alpha_i \vec{\sigma}_i\right) - \left(\vec{\sigma}_o + \sum_{i=1}^{n} \alpha_i \vec{\mu}_i\right) = \sum_{i=1}^{n} \alpha_i \left(\vec{\sigma}_i - \vec{\mu}_i\right). \tag{3.1-9}$$

Therefore, the variance of the linearly combined cross-section vector is defined by:

$$\sigma^2_{\vec{\sigma}_{LC}} = \sum_{i=1}^{n} E\left[\alpha_i^2 \left(\vec{\sigma}_i - \vec{\mu}_i\right)^2\right] = \sum_{i=1}^{n} \alpha_i^2 E\left[\left(\vec{\sigma}_i - \vec{\mu}_i\right)^2\right] = \sum_{i=1}^{n} \alpha_i^2 \sigma^2_{\vec{\sigma}_i}. \tag{3.1-10}$$

By setting $\sum_{i=1}^{n} \alpha_i^2 = 1.0$ as described above, the following holds.

$$\sigma^2_{\vec{\sigma}_{LC}} = \sum_{i=1}^{n} \alpha_i^2 \sigma^2_{\vec{\sigma}_i} \tag{3.1-11}$$

$$\sigma^2_{\vec{\sigma}_{LC}} = \sigma^2_{\vec{\sigma}} \sum_{i=1}^{n} \alpha_i^2 \tag{3.1-12}$$

$$\sigma_{\vec{\sigma}_{LC}} = \sigma_{\vec{\sigma}} \tag{3.1-13}$$

Therefore, Eq. (3.1-13) verifies that the RMS of the linearly combined cross-section vector, $\sigma_{\vec{\sigma}_{LC}}$, will be equal to a prescribed RMS of each individual cross-section vector

such that $\sigma_{\bar{\sigma}_{LC}} = \sigma_{\bar{\sigma}} \in \left[\gamma^L, \gamma^U\right]$. Finally, the standard deviation that was chosen, which exists within the lower and upper limits, can be tested by showing that,

$$\left|\left(\sum_{i=1}^{n} \alpha_i \left(\vec{y}_i - \vec{y}_o\right)\right) - \left(\vec{\Omega}\left(\vec{\sigma}_{LC}\right) - \vec{\Omega}\left(\vec{\sigma}_o\right)\right)\right| < \zeta\,, \tag{3.1-14}$$

where α_i are the scaling factors, and $\vec{y}_i$ and $\vec{y}_o$ denote some i[th] perturbed and unperturbed core attribute, respectively.

3.2 Ill-Conditioning of Covariance Data

3.2.1 Theory: Uncertainty Propagation

As seen in uncertainty quantification work by Ronen, the "sandwich rule" is an uncertainty propagation method to calculate a covariance matrix for a set of attributes given:

1) the input parameters covariance matrix
2) and the sensitivity matrix that characterizes the change in attributes per change in input parameters.

Provided with some non-linear computational model which contains input parameter uncertainties described by probability density function (PDFs), the sandwich rule is derived by taking the first and second moments of these corresponding PDFs. In this case, the input parameters uncertainties, i.e. cross-sections uncertainties, are of a Gaussian distribution. This propagation method ensures that the attributes uncertainties found by calculating the attribute covariance matrix will also have a Gaussian distribution.

Let the mathematical expectation of an arbitrary function $h\left(\vec{\sigma}\right)$ of a vector of

continuous input parameters $\vec{\sigma}$ be given by:

$$E\left[h(\vec{\sigma})\right] = \int_{-\infty}^{+\infty} h(\vec{\sigma}) f(\vec{\sigma}) d\vec{\sigma} \tag{3.2-1}$$

where $E\left[h(\vec{\sigma})\right]$ is the expected value of $h(\vec{\sigma})$ and $f(\vec{\sigma})$ is the PDF that characterizes input parameter uncertainty. Now consider a nuclear reactor core simulator's non-linear model as a vector valued function:

$$\vec{y} = \vec{\Omega}(\vec{\sigma}) \tag{3.2-2}$$

where $\vec{y} \in \Re^{m}$ is a vector of reactor performance attributes, and $\vec{\sigma} \in \Re^{n}$ a vector of cross-sections data input to the simulator. Applying Eq. (3.2-1) to the non-linear model shown in Eq. (3.2-2) provides the expected value of $\vec{y}$,

$$E[\vec{y}] = \int_{-\infty}^{+\infty} \vec{\Omega}(\vec{\sigma}) f(\vec{\sigma}) d\vec{\sigma}\,. \tag{3.2-3}$$

Further, the general definition for the covariance of these attributes is shown below:

$$COV(\vec{y}_i, \vec{y}_j) = E\left[\left(\vec{y}_i - \mu_{\vec{y}_i}\right)\left(\vec{y}_j - \mu_{\vec{y}_j}\right)^T\right], \tag{3.2-4}$$

where $\mu_{\vec{y}_*}$ represents the mean value for the $\vec{y}_*$ attribute [22]. Applying Eq. (3.2-4) to the non-linear model in Eq. (3.2-2) provides the expected covariance of the attributes,

$$COV(\vec{y}_i, \vec{y}_j) = \int_{-\infty}^{+\infty}\left[\left(\vec{\Omega}(\vec{\sigma})_i - \mu_{\vec{y}_i}\right)\left(\vec{\Omega}(\vec{\sigma})_j - \mu_{\vec{y}_j}\right)^T\right] f(\vec{\sigma}) d\vec{\sigma}\,. \tag{3.2-5}$$

Let us now perform a Taylor series expansion on Eq. (3.2-2). This expansion forms a first-order linear approximation for the non-linear model. Namely,

$$\vec{y} = \vec{y}_o + \mathbf{\Omega}\left(\vec{\sigma} - \vec{\sigma}_o\right) + O\left(\Delta^2\right) \tag{3.2-6}$$

at $\vec{\sigma} = \vec{\sigma}_o + \vec{u}$, where $\vec{y}$ is a vector of core attributes, $\vec{u}$ represents some cross-section perturbation, $\mathbf{\Omega}$ is the sensitivity matrix and $O\left(\Delta^2\right)$ are higher order terms. Further, denote $\vec{y}_\Delta = \vec{y} - \vec{y}_o$ and $\vec{\sigma}_\Delta = \vec{\sigma} - \vec{\sigma}_o$ for later use. Ideally, the sensitivity matrix can be attained by calculating the adjoint solution which reveals the sensitivity of a core attribute to all input parameters [7]. However, calculating the sensitivity matrix can be very time consuming. By neglecting higher order terms, Eq. (3.2-6) verifies that the sensitivity matrixes effect on a vector can be evaluated by running the non-linear model at two separate points where:

$$\left[\mathbf{\Omega}\right]_{ij} = \frac{\partial \vec{\Omega}\left(\vec{\sigma}\right)_i}{\partial \vec{\sigma}_j} \; for \begin{cases} i = 1,...,m \\ j = 1,...,n \end{cases}. \tag{3.2-7}$$

Substituting the first-order linear approximation of the computational model into Eq. (3.2-3) provides the mean values of the attributes, $\vec{y}_o$, where:

$$\vec{y}_o = \vec{\Omega}\left(\vec{\sigma}_o\right). \tag{3.2-8}$$

Notice that the expected value with respect to input parameters is the reference case whereas the expected value of the core attribute $\vec{y}$ is simply evaluated by running the model at the input parameters reference case. Finally, let us calculate the first-order approximate covariance for the uncertainties in $\vec{y}$ by substituting the first-order linear approximation into the general covariance equation shown in Eq. (3.2-4), where:

$$\begin{aligned} COV\left(\vec{y}_i, \vec{y}_j\right) &= E\left[\left(\mathbf{\Omega}\left(\vec{\sigma}_i - \vec{\sigma}_o\right)\right)\left(\mathbf{\Omega}\left(\vec{\sigma}_j - \vec{\sigma}_o\right)\right)^T\right] \\ &= \mathbf{\Omega} E\left[\left(\left(\vec{\sigma}_i - \vec{\sigma}_o\right)\right)\left(\left(\vec{\sigma}_j - \vec{\sigma}_o\right)\right)^T\right]\mathbf{\Omega}^T \\ &= \mathbf{\Omega} COV\left(\vec{\sigma}_i, \vec{\sigma}_j\right)\mathbf{\Omega}^T \end{aligned}. \tag{3.2-9}$$

In other words, the covariance matrix for core attribute uncertainty is given by:

$$\mathbf{C}_y = \mathbf{\Omega}\mathbf{C}_x\mathbf{\Omega}^T \tag{3.2-10}$$

where $\mathbf{C}_x$ is a block-diagonal cross-section covariance matrix that was provided by BNL [6]; each block is 15x15 corresponding to a 15 energy group representation. Figure 4 presents a graphical interpretation of a block-diagonal matrix.

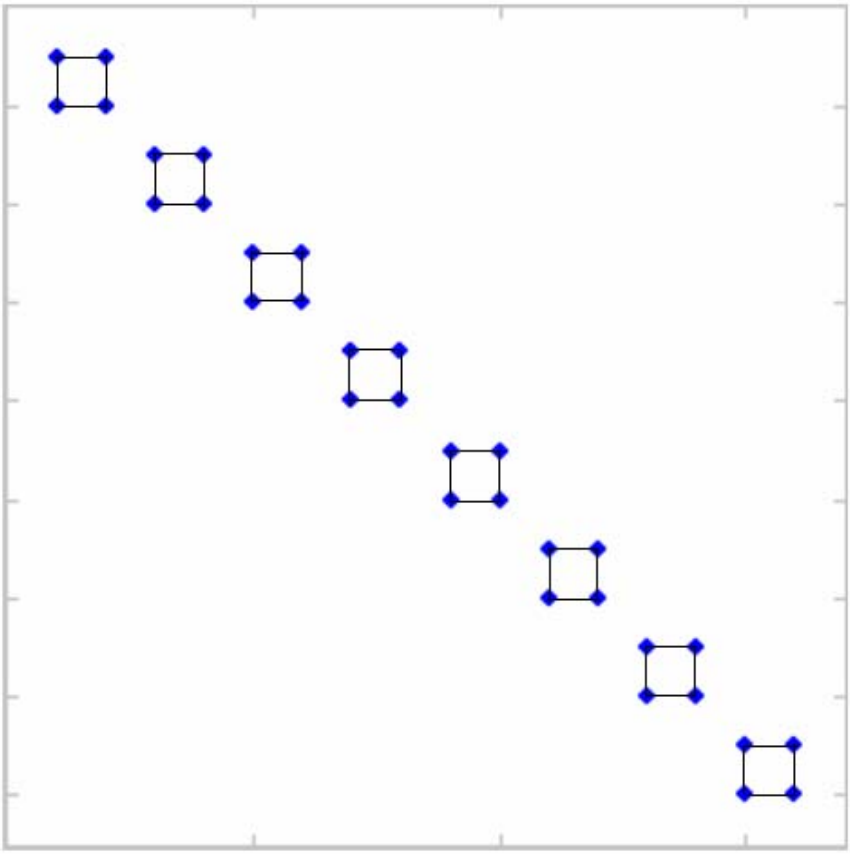

Figure 4: Block Diagonal Matrix

In this figure, let each square that is formed by the arrangement of dots represent a covariance matrix for an individual cross-section. For this study, the cross-section covariance matrix housed many more sub-covariance matrices, or blocks than shown above.

Let us also point out that any general covariance matrix, i.e. a full matrix without a trend, can be broken down into diagonals and off-diagonals. Mathematically, diagonals of a covariance matrix represent the variance of a particular attribute whereas off-diagonals represent the correlation between two different attributes. Taking the covariance of one component with respect to itself yields the variance for that specified component, where:

$$COV\left(\bar{y}_i, \bar{y}_i\right) = E\left[\left\langle \bar{y}_i - \mu_{\bar{y}_i} \right\rangle^2\right] = \sigma^2_{\bar{y}_i}. \tag{3.2-11}$$

Therefore, the diagonal entries for a given covariance matrix, i.e. the cross-section covariance matrix in this case, are in units of variance and can simply be converted into standard deviation by taking the square root of these diagonal entries.

Conventionally, uncertainty analyses attempt to create the sensitivity matrix in order to calculate the core attribute covariance matrix shown in Eq. (3.2-10); however, with large amounts of input/output (I/O) streams, using the adjoint method to create a sensitivity matrix is very time consuming and expensive, i.e. m responses would require m adjoint solutions. Therefore, a forward model approach which harnesses the strength of ESM was utilized.

3.2.2 ESM-Based Approach

In using the ESM approach, it is imperative to show how ESM builds a low rank approximation to the sensitivity or Jacobian matrix. The theory behind this approach relates to the Orthogonal Decomposition Theorem, noted in linear algebra work. This theorem shows that for every $\mathbf{\Omega} \in \Re^{m\,x\,n}$,

$$R\left(\mathbf{\Omega}\right)^{\perp} = N\left(\mathbf{\Omega}^T\right) \;\&\; N\left(\mathbf{\Omega}\right)^{\perp} = R\left(\mathbf{\Omega}^T\right) \tag{3.2-12}$$

where $\vec{\sigma}_\Delta \in \Re^n$ and $\vec{y}_\Delta \in \Re^m$.

Further, an orthogonal decomposition of $\Re^m$ and $\Re^n$ can be computed as follows:

$$\Re^m = R(\mathbf{\Omega}) \oplus R(\mathbf{\Omega})^\perp = R(\mathbf{\Omega}) \oplus N(\mathbf{\Omega}^T) \tag{3.2-13}$$

$$\Re^n = N(\mathbf{\Omega}) \oplus N(\mathbf{\Omega})^\perp = N(\mathbf{\Omega}) \oplus R(\mathbf{\Omega}^T) \tag{3.2-14}$$

where $R(*)$ denotes the range-space, $R(*^T)$ denotes the row-space, $N(*)$ denotes the null-space, $N(*^T)$ denotes the left-hand null-space, and $\oplus$ signifies that $\Re^m$ and $\Re^n$ are spaces which contain orthogonal complementary subspaces. Given that $rank(\mathbf{\Omega}) = r_\Omega$, the size for each subspace can be written as follows:

$$r_\Omega = \dim R(\mathbf{\Omega}) = \dim R(\mathbf{\Omega}^T) = n - \dim N(\mathbf{\Omega}) = m - \dim N(\mathbf{\Omega}^T) \tag{3.2-15}$$

where 'dim' stands for the dimension of $\mathbf{\Omega}$, or the number of vectors in any maximal independent subset for columns or rows of the sensitivity matrix. Eq. (3.2-15) is significant because it shows the extent of independent data present within these fundamental subspaces. Furthermore, it was shown that $\vec{\sigma}_\Delta \in \Re^n$ and $\vec{y}_\Delta \in \Re^m$; now let's apply this subspace approach to the linearly approximated model shown in Eq. (3.2-6),

$$\vec{y}_\Delta = \mathbf{\Omega}\vec{\sigma}_\Delta = \mathbf{\Omega}\left(\vec{\sigma}_\Delta^\perp + \vec{\sigma}_\Delta^\parallel\right) = \mathbf{\Omega}\vec{\sigma}_\Delta^\parallel. \tag{3.2-16}$$

Eq. (3.2-16) demonstrates that $\vec{\sigma}_\Delta \in \Re^n$ can be broken down into subspaces where, following Eq. (3.2-14), $\vec{\sigma}_\Delta^\parallel \in R(\mathbf{\Omega}^T)$, therefore $\vec{\sigma}_\Delta^\perp \in N(\mathbf{\Omega})$. The importance of this equation relates to the fact that only input data that exists in $R(\mathbf{\Omega}^T)$ can affect changes in

modeled output, such that $\vec{y}_\Delta \in R(\mathbf{\Omega})$. Therefore, the action of the sensitivity operator upon input data from $N(\mathbf{\Omega})$ will map to $\vec{0}$. Hence, data from $N(\mathbf{\Omega})$ is no longer needed and from Eq. (3.2-15) it was shown that $\dim R(\mathbf{\Omega}) = \dim R(\mathbf{\Omega}^T) = r_\Omega$. Ultimately, this reveals that only r_Ω independent input data perturbations from $R(\mathbf{\Omega}^T)$ are needed to change the output of core attributes [9],[19].

3.2.3 Mathematical Method to Calculate Core Attribute Covariance Matrix

As shown in Eq. (3.2-10), $\mathbf{C_x}$ is the cross-section covariance matrix that was provided by BNL. Previous work has illustrated that r_x, or the rank of $\mathbf{C_x}$, is often much smaller than the size of the input cross-section data and the output performance attributes, i.e. $r_x \ll n, m$, implying that only r_x forward model evaluations are required to quantify uncertainties in the attributes $\vec{y}$ [9]. The following methodology was used to prove that the cross-section covariance matrix, $\mathbf{C_x}$, is of a rank deficient form. Start by taking the singular value decomposition (SVD) of the block-diagonal matrix $\mathbf{C_x}$, which takes the form:

$$\mathbf{C_x} = \mathbf{W}\mathbf{\Sigma}_\mathbf{x}^2\mathbf{W}^\mathbf{T}, \tag{3.2-17}$$

$$\mathbf{\Sigma}_\mathbf{x}^{\,r_x \times r_x} = \mathrm{diag}\{s_j\}, \tag{3.2-18}$$

$$\mathbf{W}^{\mathbf{n} \times \mathbf{r_x}} = [\vec{w}_1 \quad \vec{w}_2 \quad .... \quad \vec{w}_{r_x}] \tag{3.2-19}$$

and $\{s_j^2\}$, and $\{\vec{w}_j\}$ are the eigenvalues and eigenvectors of the cross-section's covariance matrix. SVD is an important factorization of a real or complex matrix and due to the symmetric nature of $\mathbf{C_x}$, the right and left-hand side multiplying matrices are

equivalent. Matrix $\mathbf{W}$ contains a set of orthonormal basis vector directions for $\mathbf{C}_x$, where each $\{\vec{w}_j\}$ refers to some direction in the input data space, i.e. a perturbation of all input data that is uncorrelated with all other perturbations. Finally, the matrix $\mathbf{\Sigma}_x^2$ contains the eigenvalues which have units of variance. A cross-section perturbation matrix can now be created which aids as an input to REBUS.

$$\mathbf{X} = \mathbf{W}^{n \times r_x} \mathbf{A}^{r_x \times r_x}, \tag{3.2-20}$$

$$\mathbf{A}^{r_x \times r_x} = \text{diag}\{\alpha_j\}, \tag{3.2-21}$$

where $\mathbf{X}$ is the cross-section perturbation matrix, $\mathbf{W}$ is the left singular vector matrix from the SVD of $\mathbf{C}_x$, and $\mathbf{A}$ is a diagonal matrix composed of scalars, α_j, that fix the root mean square (RMS) for each column in $\mathbf{W}$ to a set standard deviation of $\sigma_{\vec{x}}$, or 5% to ensure that linearity of the REBUS model holds. The dimensions for the cross-section perturbation matrix are $\mathbf{X}^{n \times r_x}$, where *n* represents the total number of isotopes, reaction type, spatial composition and all 15 energy groups. Each column from $\mathbf{X}^{n \times r_x}$ is now a cross-section perturbation input file that will be run separately in REBUS. Running the perturbation matrix through REBUS produced an output matrix composed of reaction rates, which span all nodes in the core for all isotopes and fission/capture reactions, which took the form shown in Eq. (3.2-22),

$$\mathbf{Y}' = \mathbf{\Omega X}. \tag{3.2-22}$$

$\mathbf{Y}'$ is then multiplied by the corresponding eigenvalues from the SVD of the 15-group cross-section covariance matrix. The scaling factors used to fix the RMS for each column in $\mathbf{W}$ are now taken out, i.e.

$$\mathbf{Y}^{\text{m x r}_x} = \mathbf{Y}^{'}\mathbf{A}^{-1}\mathbf{\Sigma}_{\mathbf{x}}. \tag{3.2-23}$$

Using an ESM-based UQ approach [8], one can show that uncertainties in $\vec{y}$ characterized by a covariance matrix $\mathbf{C}_y$, may be given by:

$$\mathbf{C}_y = \mathbf{Y}\mathbf{Y}^{T} = \sum_{j=1}^{r_x} [\mathbf{Y}]_{*j} [\mathbf{Y}]_{*j}^{T} \tag{3.2-24}$$

where,

$$[\mathbf{Y}]_{*j} = \mathbf{\Omega}\vec{w}_j s_j = \vec{\Omega}(\vec{\sigma}_0 + \vec{w}_j s_j) - \vec{\Omega}(\vec{\sigma}_0). \tag{3.2-25}$$

Eq. (3.2-24) demonstrates how the ESM method provides another route to calculate the core attribute uncertainty covariance matrix without the explicit knowledge of the sensitivity matrix $\mathbf{\Omega}$. Matrix $\mathbf{Y}$, or the uncertainty response matrix, shown in Eq. (3.2-25) is formed simply by running the model at two points, namely at some perturbed point along with the unperturbed reference point.

Notice that the summation in Eq. (3.2-24) runs up to r_x, the numerical rank of the cross-sections covariance matrix, which is determined via a singular value decomposition. By observing the decline in the singular values from the SVD of $\mathbf{C}_x$, one can utilize the lower limit for cross-section perturbation, γ^L, to find a cutoff point at which certain perturbations contain too small of a magnitude to produce any change in core attribute output. The lower cross-section perturbation limit revealed that $r_x \ll n,m$ which proves that $\mathbf{C}_x$ is indeed ill-conditioned. Therefore, only r_x forward model evaluations are needed to evaluate the uncertainties in $\mathbf{C}_y$.

3.3 Ill-Conditioning of Model Sensitivity Matrix

Another goal of this thesis was to present a recent development of an UQ algorithm for increasing the efficiency of UQ to a level that enables its execution on a routine basis with best estimate calculations for various reactor performance attributes. To accomplish this, the latter part of this study dealt with the investigation of further reducing the amount of forward model evaluations by examining the ill-conditioned nature of the sensitivity matrix. The sensitivity matrix is a rectangular matrix that contains the first order derivatives of m core attributes with respect to n input data. Ill-conditioning of the sensitivity matrix implies that the number of independent input data perturbations leading to changes in attributes is much less than the number of input data and attributes, i.e. the matrix rank: $r_\Omega \ll n,m$, which was shown in section 3.2.2.

For this study, this proposed approach reduces the number of model evaluations to a minimum by recognizing that the rank of the covariance matrix of core attributes $\mathbf{C}_y$ is much smaller than the rank of the cross-sections covariance matrix $\mathbf{C}_x$. Again, this is due to the dimensionality reduction induced by the forward model $\boldsymbol{\Omega}$ whose numerical rank r_Ω is also shown to be very small. Following Eq. (3.2-24), it was shown that the core attribute covariance matrix could be calculated with r_x model evaluations. It is the intension of this section to prove that:

$$\mathbf{Y}\mathbf{Y}^T = \sum_{j=1}^{r_x} [\mathbf{Y}]_{*j} [\mathbf{Y}]_{*j}^T = \mathbf{C}_y = \mathbf{Y}_{\text{post}} \mathbf{Y}_{\text{post}}^T = \sum_{j=1}^{r_{post}} \left[\mathbf{Y}_{\text{post}}\right]_{*j} \left[\mathbf{Y}_{\text{post}}\right]_{*j}^T \tag{3.3-1}$$

where we can calculate the core attribute covariance matrix by capturing the effect of r_x directions while only using a linear combined subset of r_{post} directions. Section 3.3.1,

shown below, provides the algorithm that was used to calculate the core attribute covariance matrix in a reduced r_{post} forward model evaluations.

3.3.1 Algorithm to Compute Reduced Core Attribute Covariance Matrix

Studies have shown that r_{post} is smaller than the effective numerical ranks of either the sensitivity matrix or the cross-section covariance matrix, i.e. $r_{post} \le \min(r_\Omega, r_x)$. This assures that the amount of forward model evaluations to calculate the core attribute covariance matrix $\mathbf{C}_y$ can be reduced. With $r_{post} \le \min(r_\Omega, r_x)$ known, a methodology to reduce forward model evaluations to compute the core attribute uncertainty covariance matrix was created. One can exploit this by first performing an SVD factorization of the uncertainty response matrix $\mathbf{Y}$ in Eq. (3.2-25) as follows:

$$\mathbf{Y}^{m\times r_x} \simeq \mathbf{Y}_{post}^{m\times r_{post}} = \sum_{j=1}^{r_{post}} \left[\mathbf{U}_{post}\right]_{*j} \left[\mathbf{\Sigma}_{post}\right]_{jj} \left[\mathbf{V}_{post}\right]_{*j}^{T}, \tag{3.3-2}$$

where r_{post} is the effective rank of the matrix $\mathbf{Y}_{post}$. The effective numerical rank of matrix $\mathbf{Y}_{post}$ can be found by a short algorithm that will be discussed in section 4.2.1. Eq. (3.3-2) also shows that the SVD of the uncertainty response matrix $\mathbf{Y}$ is equivalent to the SVD of the reduced uncertainty response matrix, $\mathbf{Y}_{post}$. Let us now set Eq. (3.3-2) equal to Eq. (3.2-23), where one can show that:

$$\mathbf{U}_{post}\mathbf{\Sigma}_{post}\mathbf{V}_{post}^{T} = \mathbf{Y}_{post}^{m\ x\ r_{post}} = \mathbf{\Omega W \Sigma}_x, \tag{3.3-3}$$

where the effect of taking the SVD of $\mathbf{Y}_{post}$ is equal to running REBUS with r_{post} forward model evaluations. Taking the transpose of $\mathbf{V}_{post}^{T}$ on both sides of Eq. (3.3-3) yields a form that resembles Eq. (3.2-20), i.e. the cross-section perturbation matrix $\mathrm{X}^{n\ x\ r_x}$:

$$\mathbf{U}_{\text{post}}\boldsymbol{\Sigma}_{\text{post}} = \boldsymbol{\Omega}\mathbf{W}\boldsymbol{\Sigma}_{\boldsymbol{x}}\mathbf{V}_{\text{post}}, \tag{3.3-4}$$

$$\vec{z}_j = \mathbf{W}\boldsymbol{\Sigma}_{\boldsymbol{x}}\left[\mathbf{V}_{\text{post}}\right]_{*\boldsymbol{j}} \tag{3.3-5}$$

where $\vec{z}_j$ denotes the linearly combined post-processed cross-section perturbation vector. As mentioned previously, the SVD of a matrix is a type of ordered factorization that orders singular values in a descending order. In this case, the first r_{post} columns of the matrix $\mathbf{V}_{\text{post}}$ form an orthogonal basis for the fundamental subspace $R\left(\mathbf{Y}_{\text{post}}\right)$. It was found that using the first r_{post} singular vectors, or primary directions, from $\mathbf{V}_{\text{post}}$, which is used to linearly combine perturbation vectors in $z = \left[\vec{z}_1 \quad \ldots \quad \vec{z}_j\right]$, $j = 1, r_{post}$, can be evaluated through REBUS to produce similar data found from r_x forward model evaluations. Namely, from Eq. (3.2-25) and Eq. (3.3-2), one can re-write Eq. (3.2-24) as:

$$\mathbf{C}_y = \sum_{\boldsymbol{j}=1}^{\boldsymbol{r}_{\text{post}}}\left[\mathbf{Y}_{\text{post}}\right]_{*\boldsymbol{j}}\left[\mathbf{Y}_{\text{post}}\right]_{*\boldsymbol{j}}^{\boldsymbol{T}}, \tag{3.3-6}$$

where

$$\left[\mathbf{Y}_{\text{post}}\right]_{*\boldsymbol{j}} = \vec{\Omega}(\vec{\sigma}_0 + \vec{z}_j) - \vec{\Omega}(\vec{\sigma}_0). \tag{3.3-7}$$

At this point in the derivation, the core attribute covariance matrix was calculated using reduced r_{post} forward model evaluations. It is also shown in Eq. (3.3-7) that $\mathbf{Y}_{\text{post}}$ was calculated using the derived linearly combined cross-section perturbation vector from Eq. (3.3-5). Finally, substituting the SVD of $\mathbf{Y}_{\text{post}}$, which is shown in Eq. (3.3-2), into Eq. (3.3-6) yields an equation that calculates $\mathbf{C}_y$, where

$$\mathbf{C}_y = \sum_{\boldsymbol{j}=1}^{\boldsymbol{r}_{\text{post}}}\left[\mathbf{U}_{\text{post}}\boldsymbol{\Sigma}_{\text{post}}\mathbf{V}_{\text{post}}^{\boldsymbol{T}}\right]_{*\boldsymbol{j}}\left[\mathbf{V}_{\text{post}}\boldsymbol{\Sigma}_{\text{post}}\mathbf{U}_{\text{post}}^{\boldsymbol{T}}\right]_{*\boldsymbol{j}}. \tag{3.3-8}$$

However, computational time associated with the calculation of $\mathbf{C}_y$ shown in Eq. (3.3-8) is high due to the fact that $m \gg r_{post}$, where $\mathbf{C}_{\mathbf{y}} = \left[\mathbf{Y}_{\text{post}}^{\text{m x r}_{\text{post}}}\right]\left[\mathbf{Y}_{\text{post}}^{\text{m x r}_{\text{post}}}\right]^T$. This matrix times matrix operation requires $\left\{m^2 * r_{post}\right\} + \left\{m^2\left(r_{post} - 1\right)\right\}$ multiplication and addition operations. By realizing the orthogonal nature of $\mathbf{V}_{\text{post}}$, where $\mathbf{V}_{\text{post}}^{\mathbf{T}} = \mathbf{V}_{\text{post}}^{-1}$, Eq. (3.3-8) simplifies to

$$\mathbf{C}_y = \sum_{j=1}^{r_{\text{post}}} \left[\mathbf{U}_{\text{post}} \boldsymbol{\Sigma}_{\text{post}}^2 \mathbf{U}_{\text{post}}^{\boldsymbol{T}}\right]_{*j}. \tag{3.3-9}$$

Recall that all input data, denoted by $\bar{\sigma}$, are contained where $\bar{\sigma} \in \Re^n$. Note that the size of the input data space is n, whereas the sources of uncertainty have been reduced to r_{post}, i.e. the effective rank of $\mathbf{C}_y$. Therefore, Eq. (3.3-9) shows that core attribute uncertainties can be calculated via r_{post} forward model evaluations compared to the former $r_x << n$ evaluations by use of the singular vector and singular value matrices, $\mathbf{U}_{\text{post}}$ and $\boldsymbol{\Sigma}_{\text{post}}^2$, respectively.

3.4 Uncertainty Quantification

3.4.1 Key Attribute Uncertainties Quantification

At this point in the study, an efficient algorithm which utilizes the ESM techniques has been completed to calculate the core attribute uncertainty matrix with $\boldsymbol{r}_{\text{post}}$ forward model evaluations. It is of further interest to utilize this algorithm to quantify the uncertainties for specific reactor core attributes that greatly affect core performance and safety. Formulating these core attribute uncertainties is ideal for fast reactor design and implementation. Not only will the knowledge of these uncertainties aid in future fast

reactor work, but increase profits by reducing design margins between operating and limiting parameters via reactor design optimization and experimentation. Such core attributes for the ABTR include discharge burnup, conversion ratios, and power peaking factors, to name a few. These quantities, along with more attributes, will be the primary focus for uncertainty quantification.

Let $\tilde{y}_o^l$ denote an unperturbed key core attribute that was either calculated or documented in this study. It was previously found and shown in Eq. (3.3-6) that the core attribute covariance matrix $\mathbf{C}_y$ can be calculated in reduced r_{post} forward model evaluations. Now set some perturbed response, $\tilde{y}_i^l$ which exist in $\mathbf{Y}_{\text{post}}$, for $l = 1,\ m$ where m denotes total number of responses. Arbitrarily setting $\mathbf{C}_y$ to contain only one response allows us to generate an equation to calculate core attribute uncertainty. Begin by subtracting then dividing each perturbed response by the nominal value to form a relative quantity:

$$\hat{y}_i^l = \frac{\tilde{y}_i^l - \tilde{y}_o^l}{\tilde{y}_o^l}, \quad \text{for} \begin{cases} i = 1,\ r_{post} \\ l = 1,\ m \end{cases} \tag{3.4-1}$$

where $\hat{y}_i^l$ denotes a relative response for run 'i' and response 'l'. Applying the same principles used in Eq. (3.2-23), the linearity normalization factors from matrix $\mathbf{A}$ that were used in pre-processing work, α, must be taken out to accurately calculate any uncertainty, i.e.,

$$\hat{y}_i^l = \frac{\tilde{y}_i^l - \tilde{y}_o^l}{\tilde{y}_o^l * \alpha_i}. \tag{3.4-2}$$

Given that $\mathbf{C}_y$ has been arbitrarily set to contain one response, Eq. (3.3-6) is now a vector-row multiplied by vector-column operation. In linear algebra terms, this equates to the squared Euclidean norm which can be seen in Eq. (3.4-3),

$$\begin{aligned} \mathbf{Y}_{\text{post}}\mathbf{Y}_{\text{post}}^{T} &= \sum_{i=1}^{r_{post}}\left(\tilde{y}_i^l\right)^2 \\ \Rightarrow \sigma_{\hat{y}^l}^2 &= \sum_{i=1}^{r_{post}}\left(\frac{\tilde{y}_i^l - \tilde{y}_o^l}{\tilde{y}_i^l * \alpha_i}\right)^2 . \end{aligned} \tag{3.4-3}$$

Therefore, the uncertainty for any key core attribute was found by taking the square root of Eq. (3.4.3):

$$\sigma_{\hat{y}^l} = \sqrt{\sum_{i=1}^{r_{post}}\left(\frac{\tilde{y}_i^l - \tilde{y}_o^l}{\tilde{y}_i^l * \alpha_i}\right)^2} . \tag{3.4-4}$$

3.4.2 Identification of Key Uncertain Cross-Sections

As mentioned in the introduction to this thesis, one goal of this study was to identify the key isotopes/reaction type combination that contributed the most to these calculated uncertainties. By taking the forward model approach, a single input parameter can be perturbed which in turn affects all output data. Hence, this method allows one to pinpoint key input data that contributes to higher core attribute uncertainty. Recall that Eq. (3.2-17) presents the SVD of the block-diagonal cross-section covariance matrix $\mathbf{C}_x$, where matrices that contain the eigenvalues and eigenvectors for $\mathbf{C}_x$ are presented in Eq. (3.2-18) and Eq. (3.2-19), respectively. Additionally, these eigenvalues correspond to isotopes with specific reaction types that exist in a range of energy groups. One can show that these eigenvalues represent an uncertainty for each isotope/reaction rate combination.

Furthermore, a methodology, described below, which harnesses the standard deviation of diagonal entries from the cross-section covariance matrix, was used to identify the important cross-sections that contribute to high core attribute uncertainty. Taking the SVD of the uncertainty response matrix $\mathbf{Y}^{m \times r_x}$ in Eq. (3.2-23) reveals a similar form seen in Eq. (3.3-1) with the reduced r_{post} evaluations. The importance of this factorization lies with the right-hand singular vector matrix $\mathbf{V}$ which is composed of r_{post} orthonormal column vectors. Due to the factorization techniques of the SVD, higher level importance vectors are placed from left to right in $\mathbf{V}$. Therefore, by ordering the first column in $\mathbf{V}$ from high to low, the corresponding singular values can also be ordered with the same index. Thus, this technique provides a descending ordered list of isotopes with specific reaction types that exist at a certain energy group with corresponding uncertainty values.

4 Results

4.1 Model Linearity

Before utilizing this ESM based methodology for uncertainty quantification of key core attributes for this ABTR design, a linearity study was performed on a non-linear fast reactor fuel cycle model. Recall from section 3.1 that the ESM method can be employed assuming that the computational model behaves linearly within range of input data uncertainties; two linearity studies were presented in section 3.1 to ensure that.

4.1.1 Scaled Random Cross-Section Perturbation Study

The first linearity test consists of scaling the cross-section perturbations vectors, which are randomly generated, by factors ranging from zero, denoting no cross-section perturbation, to five times their initial standard deviation, set to be 5% for all perturbations vectors. By plotting core attribute deviations from the unperturbed case one can determine if the model behaves linearly with cross-sections perturbations. For this linearity study, two core attributes were selected, the multiplication factor, and reaction rates. The multiplication factor k_{eff} is defined by:

$$k_{eff} \equiv \frac{\text{Number of neutrons in generation (n)}}{\text{Number of neutrons in generation (n-1)}}, \tag{4.1-1}$$

also referred to as core reactivity; the multiplication factor is a global reactor performance metric that describes the balance of neutrons, a core reactivity of 1.0 implies that neutrons are produced and lost at the same rate thus ensuring a self-sustained controlled chain reaction. Following Eq. (3.1-2), cross-section perturbation vectors were scaled by scaling factor, $\alpha \in [0,5]$. Figure 5 plots these scaling versus the k_{eff} deviations

at the end of cycle, i.e. [Perturbed-DC] data collected for this study. Let 'DC' denote the unperturbed case.

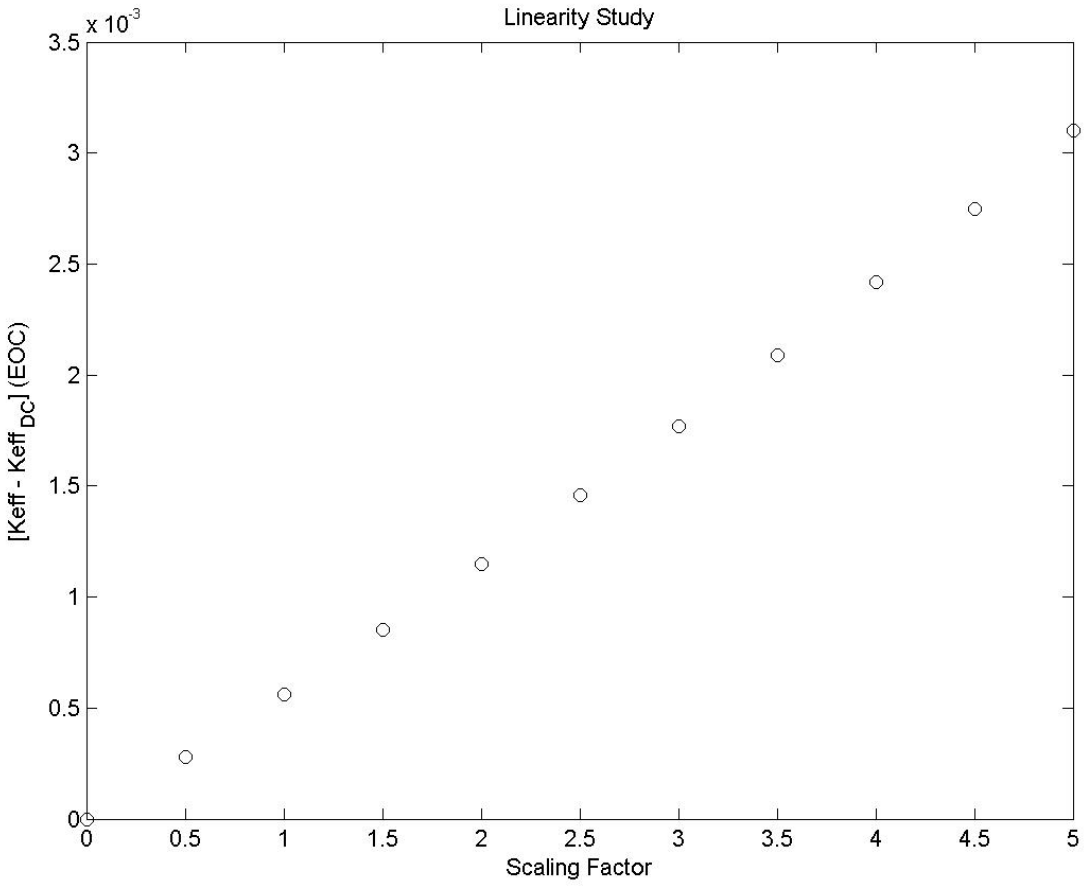

Figure 5: Linearity Test A: Normalized keff vs. Scaling Factor at EOC

It is evident from Figure 5 that as the standard deviation is scaled from $[0,5]$ the absolute change in k_{eff} taken at EOC increases linearly. To create an unbiased approach to cross-section perturbation, multiple randomly generated vectors were employed to repeat the previous study and model local linearity was observed. Figure 6 repeats the plot in Figure 5 but for another random perturbation vector showing a decrease in k_{eff}.

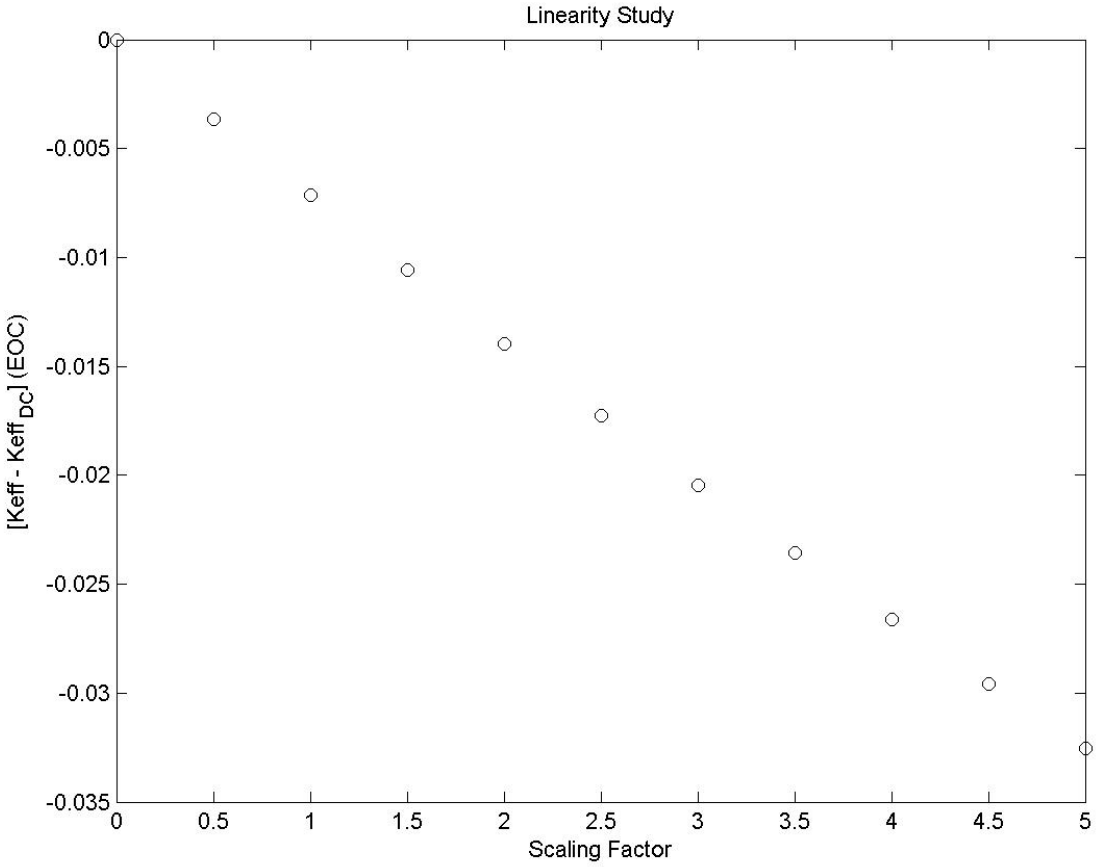

Figure 6: Linearity Test B: Normalized keff vs. Scaling Factor at EOC

The second class of core attributes considered are the fission and absorption reaction rates at various locations inside the core. Figure 7 plots the reaction rates deviations at various core locations vs. scaling factor at EOC in a similar manner to the previous graphs.

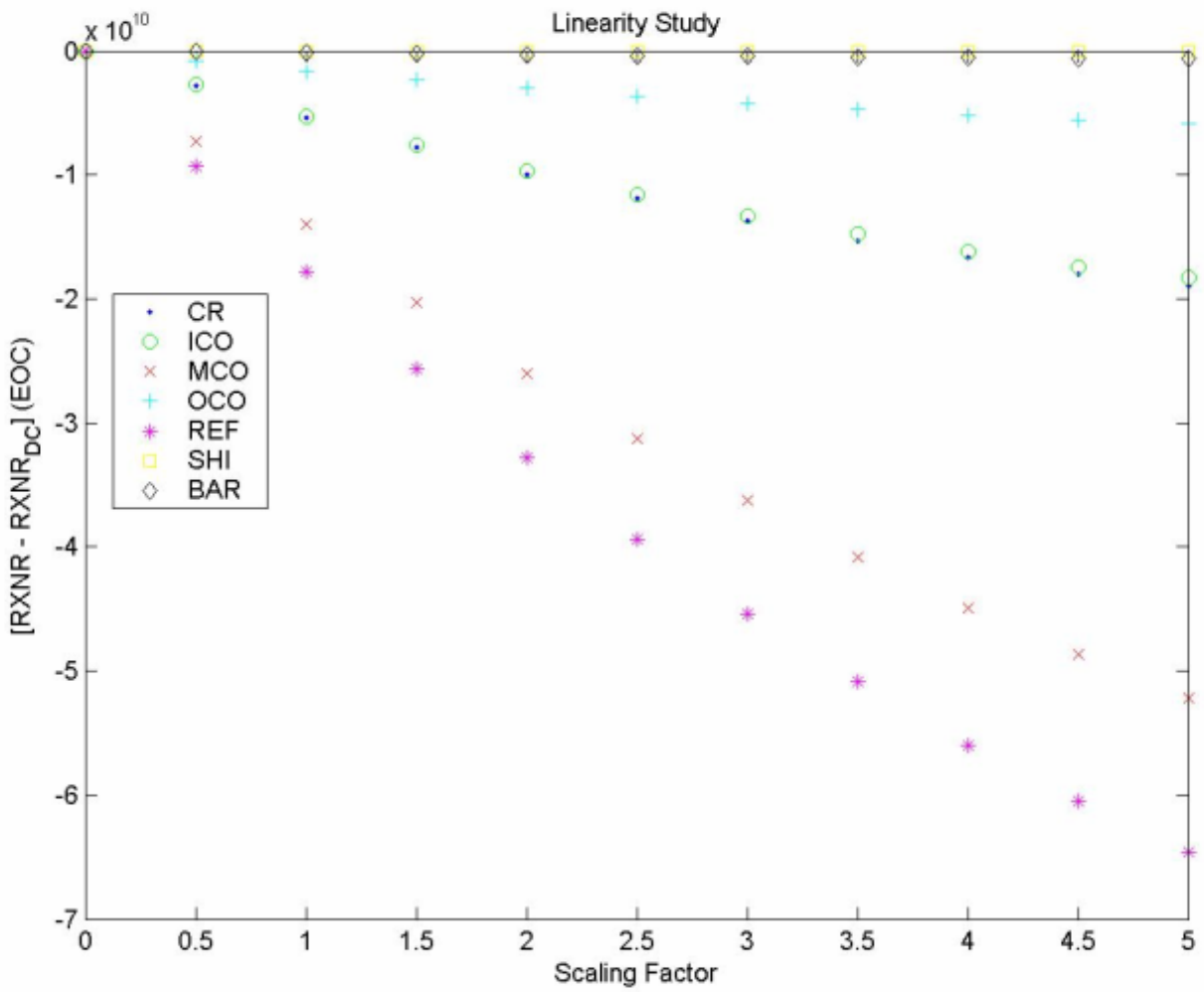

Figure 7: Linearity Test C: Normalized Node Reaction Rate vs. Scaling Factor at EOC

The legend in the top-left corner describes the core regions for which the reaction rates deviations are plotted, i.e. 'CR', 'ICO', 'MCO', 'OCO', 'REF', 'SHI', and 'BAR' denote control rod, inner-core, middle-core, outer-core, reflector, shield and barrel regions, respectively. Again, these figures demonstrate the linearity of the reaction rates variations within the range of introduced cross-sections perturbations. Figure 7 only presents one reaction rate value for each region for the sake of simplicity. For this study, the number of reaction rates is on the order of 2e4 and would present a crowded graph

representation. Therefore, the linearity of all reaction rates was confirmed and only a few reaction rates were arbitrarily chosen to represent each core region.

After conducting these linearity tests with different random directions, the lower and upper limits for cross-section perturbation could be found via the use of the prescribed numerical tolerance limit. Based on thermal reactor analysis experience [4], the numerical tolerance limit was set to 10 pcm and 0.1% for reactivity and core power density, respectively. Table 3 shows the results for the lower and upper cross-section perturbation limits.

Table 3: Cross-Section Perturbation Limit

Cross-Section Perturbation Limit (Standard Deviation)	
Lower Limit - γ^L	**Upper Limit - γ^U**
0.01%	7.50%

Both the lower and upper cross-section perturbation limits that were calculated for this study were quite conservative. Following Eq. (3.1-4), the point at which the LHS became less than the numerical tolerance limit was the point at which the lower limit for cross-section perturbation was found. In other words, after normalizing the perturbed core attribute from the unperturbed case, a standard deviation of 0.01% was the point at which the modeled response was greater than the non-linear error margin. It was also found that applying a 0.01% standard deviation for cross-section perturbation was large enough to produce a noticeable change in core attributes. Further, the upper limit was calculated via Eq. (3.1-3). This equation states that the upper limit for cross-section perturbation will be found when the difference in the perturbed core attribute from the unperturbed case

exceeds the numerical tolerance limit. And, the residual of Eq. (3.1-3) is denoted as the non-linear error margin which should not exceed the numerical tolerance limit. It was found that an upper limit of 7.50% was the standard deviation for cross-section perturbation that would conserve model local linearity.

4.1.2 Multiple Random Cross-Section Perturbation Study

The second study to check model local linearity was to once again allow a random number generator to produce random perturbation vectors; however, in this case there will be many different random vectors instead of only using one. As mentioned in the methodology section of this thesis, to ensure linearity, one must show that if there are *n* random directions and their corresponding attributes deviation, then a linearly combined vector, which is the weighted sum of the random vectors must induce deviations in the attributes that can be written as a linear combination of the original *n* attributes perturbations using the same weights used to combine the random vector. In this instance, k_{eff} values at EOC along with nodal power density data were used to check the linear range of the model. Table 4 shows the data collected from applying this linearity study with k_{eff} data at EOC.

Table 4: Combined Linearity Test: Perturbed keff Data at EOC

Run	k_{eff}
1	0.98723
2	0.98061
3	0.97604
4	0.98393
5	0.98132
6	0.97787
7	0.98605
8	0.97595
9	0.98384
10	0.97956
11	0.98675
Linearly Combined	0.98157
Compare	0.98161549
Error	4.634412217 pcm

It can be seen in Table 4 that there are 11 runs along with the linearly combined run. The k_{eff} column is a list of k_{eff} at EOC data collected for each random direction with a standard deviation of 5%. The linearly combined perturbation vector was run through REBUS and thus a corresponding k_{eff} value at EOC was calculated. Following Eq. (3.1-14), this technique will either prove or disprove that REBUS is linear for this standard deviation of 5% by manually calculating the combined k_{eff} value. This is done by taking each of the 11 k_{eff} values and multiplying them by random scaling factors and summing these together. Recall, that the summation of the square of each random scaling factor was equal to 1.0. This was performed and is shown as the 'Compare k_{eff}' value in Table 4. The error shown in Table 4 was found by calculating $\frac{\Delta k}{k}$ between the 'Linearly Combined and Compare k_{eff}' values and converting to pcm. Ultimately, the error between the 'Linearly Combined and Compare' case was less than the prescribed

numerical tolerance limit of 10 pcm, which proves that REBUS conserved linearity with a standard deviation of 5%.

Provided with the same randomly created scaling factors used in the calculation shown in Table 4, Figure 8 shows the linearity study data collected for nodal power density over the active fuel region.

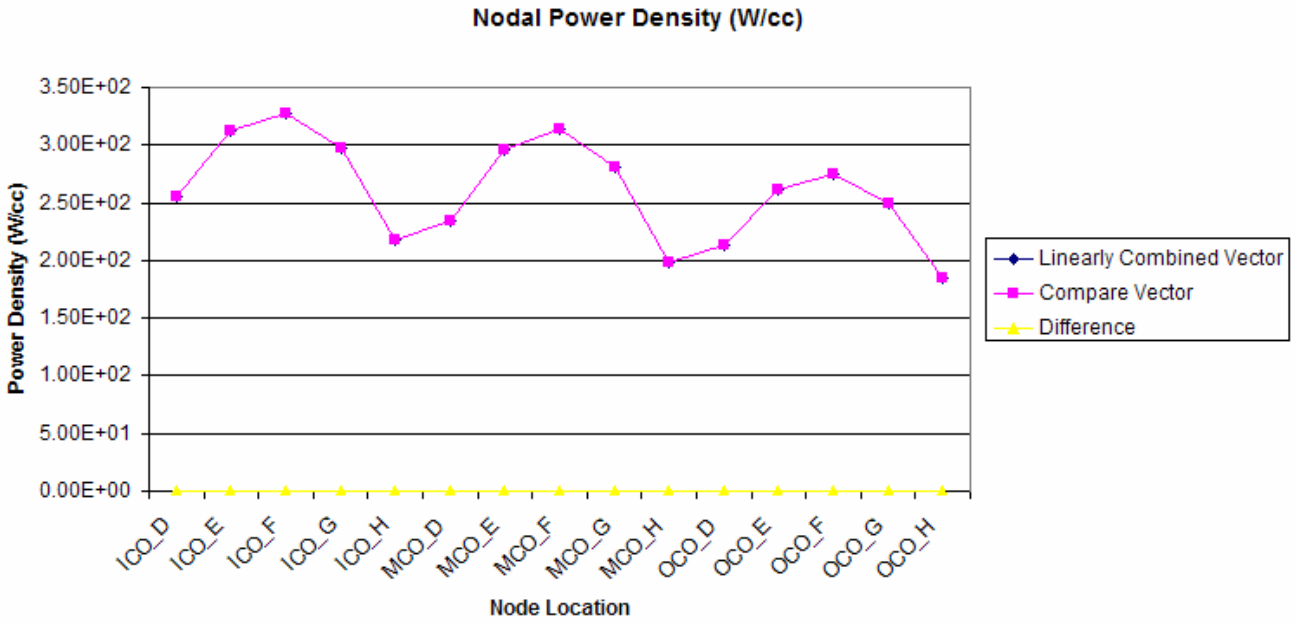

Figure 8: Nodal Power Density in Active Core Region

This study primarily focuses on core attributes, therefore only nodes in the inner, middle and outer regions of the active fuel region were selected. Starting at the bottom of the core, let the variables "D-H" denote axial slices in the active fuel region. Following Eq. (3.1-5), the linearly combined case was created and the output from this run is presented as the linearly combined vector in Figure 8. Further, by manually creating a linearly combined vector using power density data along with the randomly created scaling factors, a comparison vector was created to check against the linearly combined vector. Finally, the error between the linearly combined and compare case needed to be less than

the set numerical tolerance limit of 0.1% for active core power density nodes to conserve model linearity. The error between the linearly combined and compare vectors is shown in yellow in the plot and is less than the prescribed tolerance limit. Therefore, setting the cross-section perturbation standard deviation at 5% ensures that model local linearity is conserved and validates the condition so that the ESM based algorithm can be utilized.

4.2 Ill-Conditioning of Covariance Data & Model Sensitivity Matrix

For this study, an unofficial release of a 15-group cross-section covariance matrix from BNL, denoted by $\mathbf{C}_x$ was utilized [6]. Following the methodology in section 3.2, it was estimated that the rank of the cross-section covariance matrix was much less than the size of this matrix, and the output core attributes, i.e. $r_x \ll n,m$; this implies that only r_x forward model evaluations are required to quantify uncertainties in the attributes $\vec{y}$.

Further, the methodology in section 3.3 discusses the work to further reduce the amount of forward model evaluations to a minimum by recognizing that the rank of the core attribute covariance matrix $\mathbf{C}_y$ is much smaller than the rank of the cross-sections covariance matrix $\mathbf{C}_x$. Following Eq. (3.3-6), the numerical rank of $\mathbf{C}_y$ can only be equivalent to the rank of the uncertainty response matrix $\mathbf{Y}_{\text{post}}$. Taking the SVD of $\mathbf{Y}_{\text{post}}$ led to a discovery that only r_{post} forward model evaluations were necessary to reproduce $\mathbf{C}_y$.

By observing the decline of singular values that were found by taking the singular value decomposition of $\mathbf{C}_x$ and $\mathbf{Y}_{\text{post}}$, one can find a point at which the cross-section perturbation is too minimal to produce a noticeable change in key core attribute output.

Figure 9 shows the square-rooted singular values for cross-section and core attribute output covariance matrices, $\mathbf{C}_x$ and $\mathbf{C}_y$, respectively.

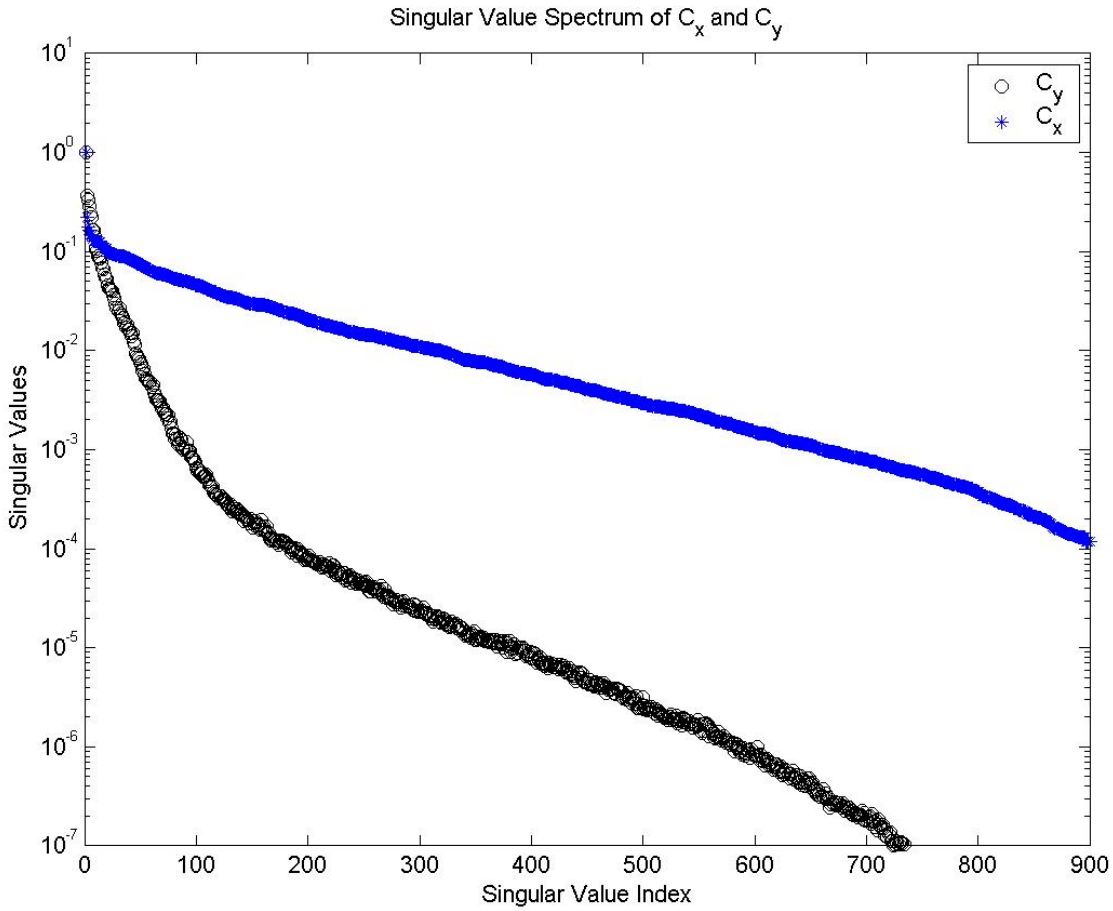

Figure 9: Covariance Matrices Cx and Cy Singular Value Spectrum vs. Index

The singular value spectrum of $\mathbf{C}_x$ and $\mathbf{C}_y$ is shown in units of percentage standard deviation. Also, all singular values for each corresponding matrix have been normalized so that the largest value is set to 1.0. For this study, an effective rank of the matrix $\mathbf{C}_x$ was chosen such that $r_x = \mathbf{900}$. Based on the lower limit $\gamma^{\mathrm{L}} = 0.01\%$, Figure 9 reveals that an effective rank $r_x \approx 300$ is appropriate. However, by setting the rank of the cross-

section covariance matrix well above the lower limit, a more conservative approach could be taken.

Alternatively, the faster decline of the singular values from $\mathbf{C}_y$ indicates the rank reduction induced by the action of the forward model. This figure implies that the rank of the core attributes covariance matrix is much smaller than its dimensions, and hence one can exploit this to reduce the number of forward runs even further.

4.2.1 Algorithm to Calculate r_{post} Numerical Value

It was shown in Eq. (3.3-1) that the core attribute covariance matrix could be created by either using r_x or a linearly combined r_{post} forward model evaluations. Further, let us recall that Eq. (3.3-9) revealed an efficient way to calculate the core attribute covariance matrix. The following algorithm was used to calculate the numerical value of r_{post}.

1. Given that: $\mathbf{C}_y = \sum_{j=1}^{r_x} [\mathbf{U}]_{*j} [\mathbf{\Sigma}]_{jj}^2 [\mathbf{U}]_{*j}^T$.

2. Calculate: $\sigma_{y_i}^2 \{r_x\} = \sum_{j=1}^{r_x} [\mathbf{U}]_{ij}^2 [\mathbf{\Sigma}]_{jj}^2$, $i = 1,\ m$.

3. Set: r_{post}=1.

4. Calculate: $\sigma_{y_i}^2 \{r_{post}\} = \sum_{j=1}^{r_{post}} [\mathbf{U}]_{ij}^2 [\mathbf{\Sigma}]_{jj}^2$.

5. If

$$\left(\frac{\sigma_{y_i}^2 \{r_{\text{post}}\} - \sigma_{y_i}^2 \{r_x\}}{\sigma_{y_i}^2 \{r_x\}} \right) * 100\%,\ i = 1,\ m \ \leq\ 0.01\% \quad \begin{cases} \text{YES: Goto Step 6.} \\ \text{NO: Goto Step 3. Set } r_{\text{post}} = r_{\text{post}} + 1 \end{cases}$$

6. Algorithm complete.

The overall concept of this algorithm is to calculate the effective rank of the core attribute covariance matrix that will ultimately fulfill Eq. (3.3-1). To begin, let us denote brackets $\{\ \}$ shown in steps 2 and 4 as simple notation which signifies that either r_x or r_{post} evaluations were used. The algorithm starts with a r_{post} guess of 1 and continues to build until step 5 has been met. As shown in step 5 above, r_{post} is found when the percent difference between the core attribute variance calculated with r_x and r_{post} evaluations is less than or equal to the prescribed numerical tolerance limit. This limit is set above the non-linear error margin and is based on engineering judgment pertaining to this study. Via this methodology, the effective numerical rank of $\mathbf{C}_y$ was found where $r_{post} = \mathbf{50}$.

Figure 10 presents the unperturbed reaction rate data that was calculated for this study. Figure 11 compares the relative uncertainties calculated for reaction rates with r_x and r_{post} forward runs, respectively.

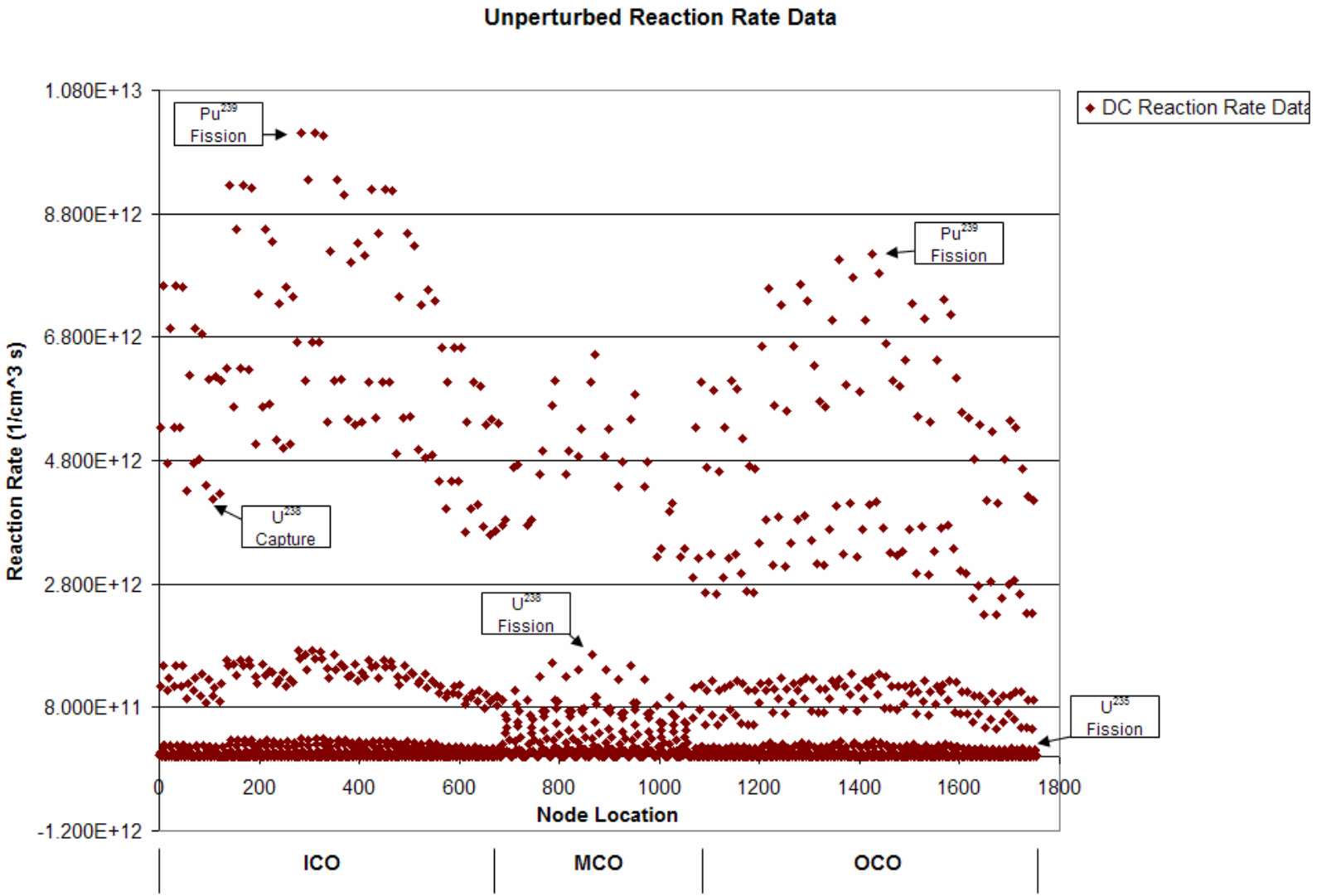

Figure 10: Unperturbed Reaction Rate Data vs. Ordered Nodal Location

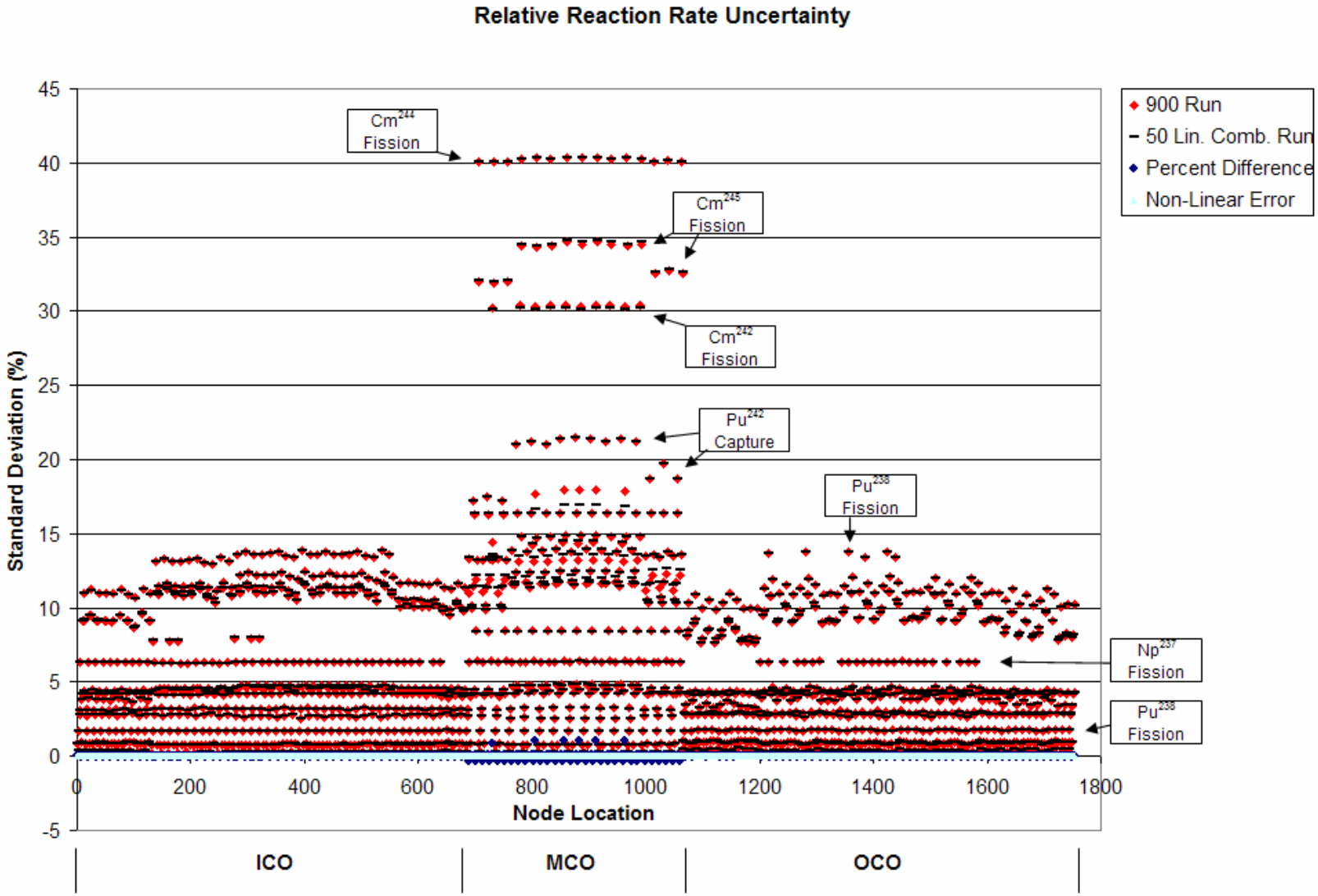

Figure 11: Relative Reaction Rate Uncertainty vs. Ordered Nodal Location

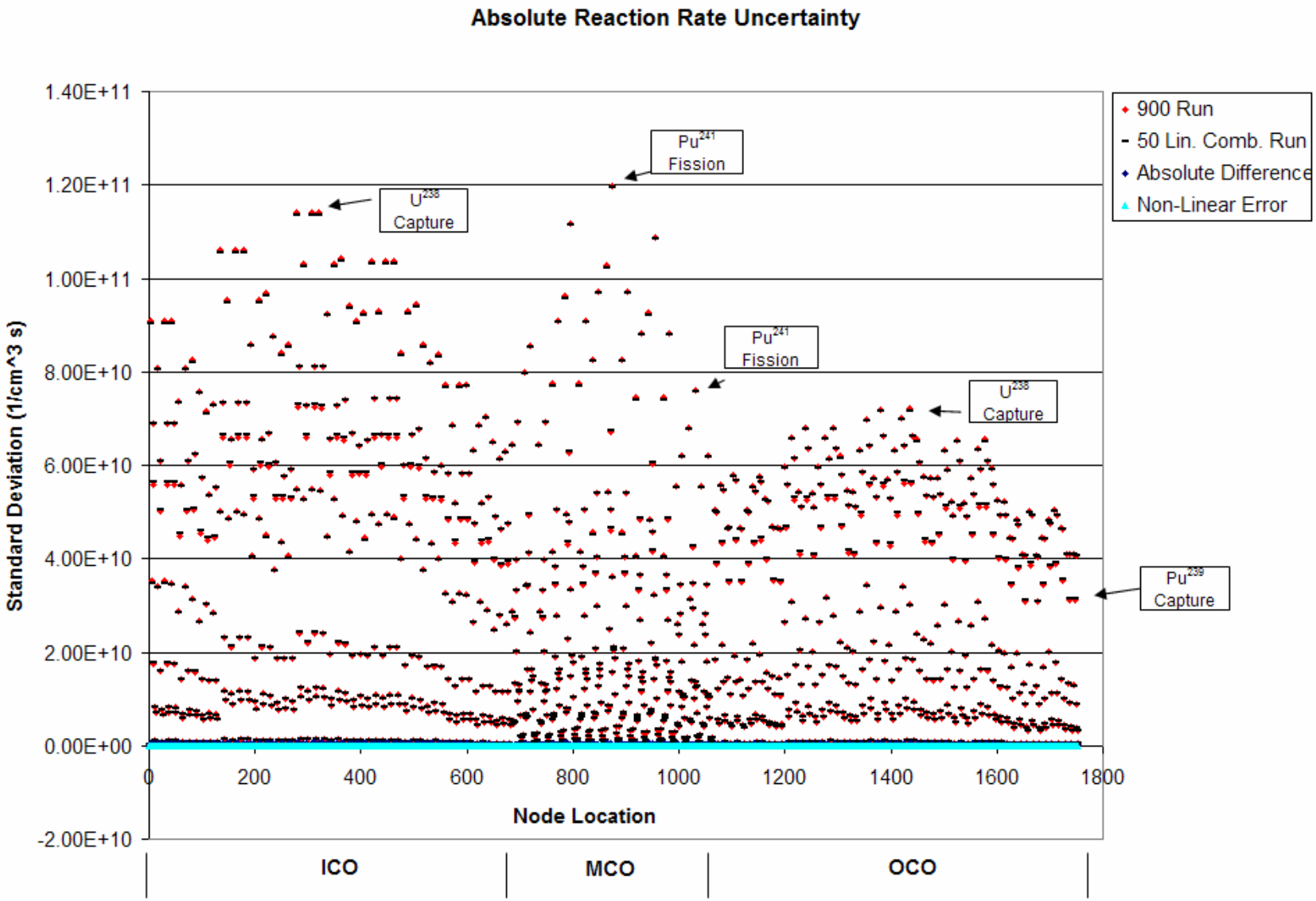

Figure 12: Absolute Reaction Rate Uncertainty vs. Ordered Node Location

Previously, it was mentioned that reaction rates were calculated for every node in the core for every isotope that could experience fission or capture reactions within a specific energy range. However, it is not necessary to plot isotopes that exist in the structural components or coolant region of the core for a fast neutron spectrum. Appendix 1 presents neutron capture and/or neutron absorption cross-section plots for these isotopes that exist in the structural components and coolant region to confirm that such cross-section data are negligible in a fast spectrum. So, Figure 10, Figure 11 and Figure 12 present the unperturbed reaction rates, relative reaction rates uncertainties and absolute reaction rate uncertainties that were calculated at each node location only within the active fuel region of the core for (U, Pu, Np, Am, Cm) isotopes which experience fission and capture reactions. The x-axes of Figure 10 and Figure 11 denote ordered node location, where these nodes run over axial planes (D-H) and all radial nodes within the core. Further, both x-axes are divided into three node location regions to graphically present the unperturbed reaction rates and reaction rates uncertainties throughout these segments of the core. Let 'ICO', 'MCO' and 'OCO' denote inner-core, middle-core and outer-core regions, respectively. The neutron flux spectrums for these regions can be found in Appendix 2. As expected, the unperturbed reaction rates due to these isotopes are higher in the inner-core and outer-core regions; whereas, reaction rates in the middle-core region are much lower. This result is due to LWR-SF TRU fuel being used in the middle-core assemblies where as the inner-core and outer-core assembles contain high fissile WG-Pu fuel assemblies. The TRU isotopic concentration for these two different fuel assemblies can be found in Table 1.

Figure 11 presents the relative reaction rate uncertainties that were calculated for this core design via Eq. (3.3-9). Additionally, note that this figure is broken down into four separate plots for comparison purposes. The legend shown in the top-right corner presents a brief description about each plot. The red data represents reaction rate uncertainty that was calculated using all 900 primary directions from $\mathbf{C}_x$. Alternatively, the black data, which greatly matches the former, represents reaction rate uncertainties that were calculated using the 50 linearly combined post-processed cross-section perturbation vectors that were calculated using Eq. (3.3-5). The ultimate scope of this plot is to examine the difference between these two uncertainty cases. Therefore, the percent difference data between the 900 and 50 cases is plotted in dark blue.

As shown in Figure 11, the relative reaction rate uncertainty is highest in the middle-core region compared to the inner-core and outer-core regions. Additionally, labels were placed into Figure 11 to point out which reactions were causing these higher uncertainties. It was found that reaction rates of ^{244}Cm (n,f), ^{245}Cm (n,f), ^{242}Cm (n,f), ^{242}Pu (n,γ) and ^{238}Pu (n,f) reactions have the highest relative uncertainties in the middle-core region. This result is due to the TRU isotopic composition that is shown in Table 1. It can be seen that higher amounts of Pu, Am, and Cm isotope percentages are present in the LWR-SF TRU fuel, whereas zero parts of Am and Cm are integrated into the inner-core and outer-core WG-Pu assemblies. Also note that the Cm isotopes reaction rates have the highest relative uncertainties since they have the highest relative cross-sections uncertainties as given in Figure 13 and Figure 14 in absolute and relative terms.

The residual to Eq. (3.1-1), or the non-linear error was plotted in light blue in Figure 11. In an ideal case, this model would be linear and non-linear error would not

exist. As the degree of non-linearity increases in a model, calculated uncertainties become more of an approximation rather than accurate responses. The model for this study is indeed non-linear; however, it can be seen in Figure 11 that the non-linear error is negligible and is contained within the span of the reaction rate uncertainty data. This signifies that the non-linear error present in the model will not affect the accuracy of these calculated uncertainties.

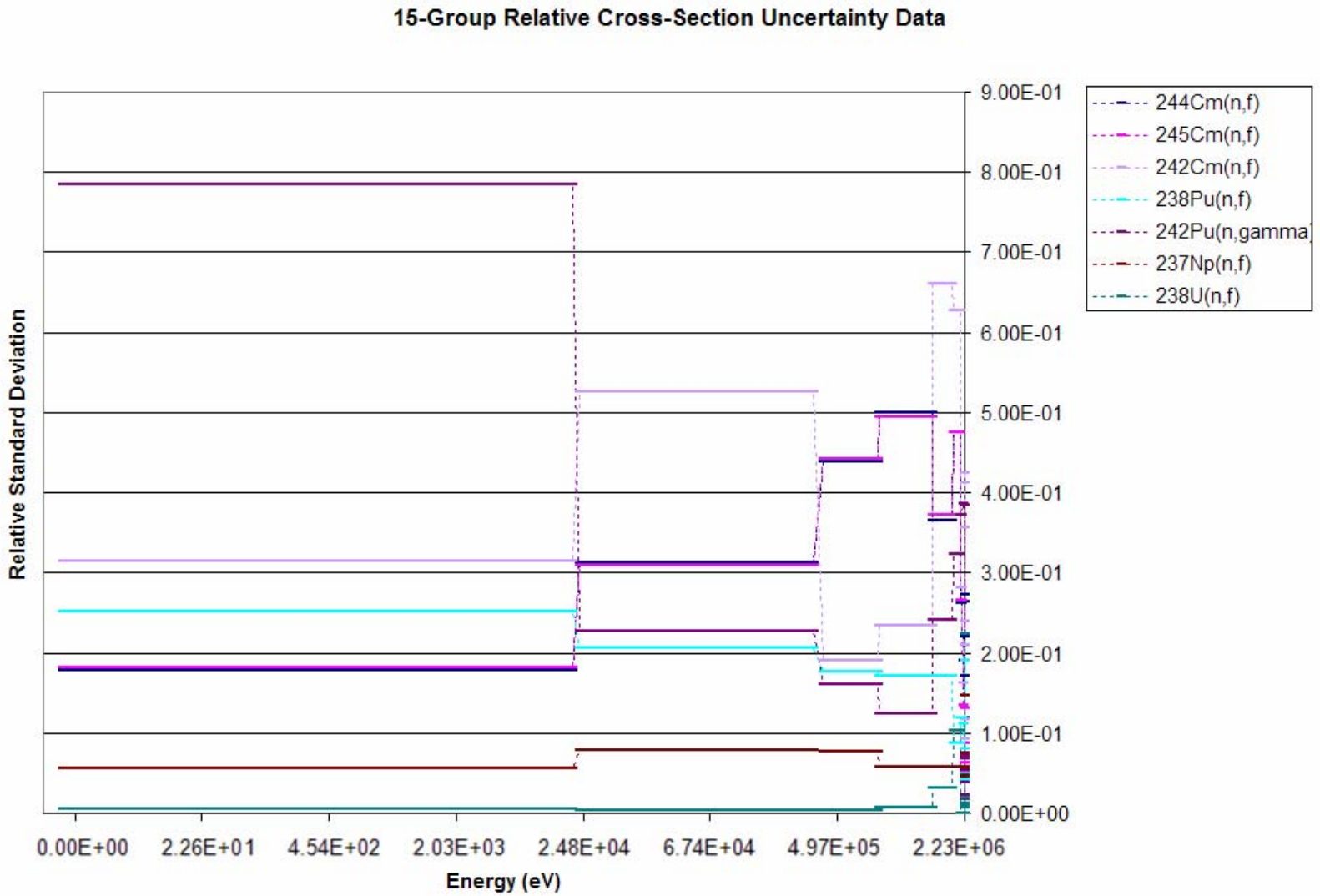

Figure 13: 15-Group Relative Cross-Section Uncertainty Data

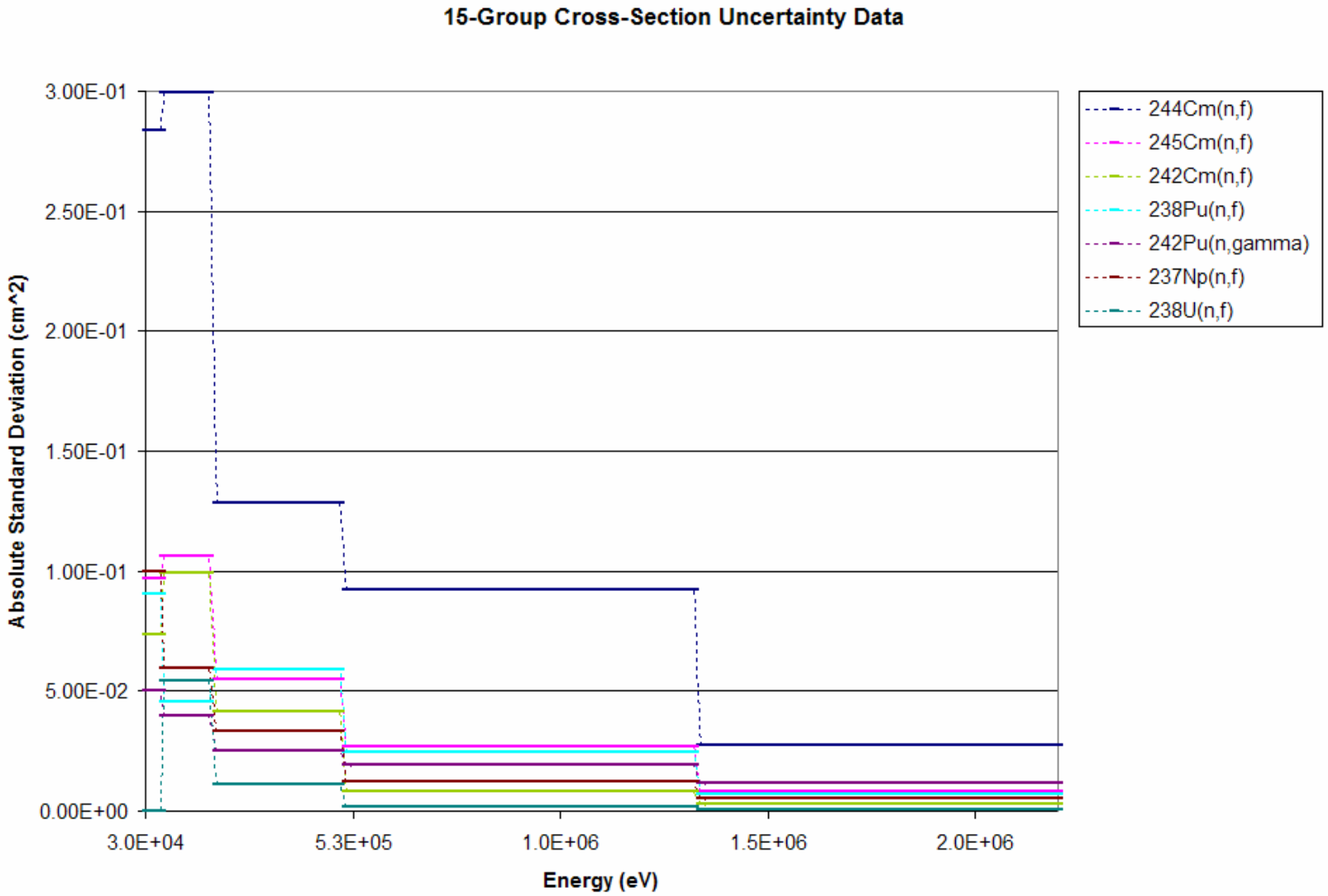

Figure 14: 15-Group Absolute Cross-Section Uncertainty Data

4.3 Uncertainty Quantification

4.3.1 Key Attribute Uncertainty Quantification

After the discovery that reduced r_{post} forward model evaluations were sufficient to calculate the core attribute uncertainty matrix $\mathbf{C}_y$, it was beneficial to apply these r_{post} runs to calculate uncertainties in key core attributes. The key core attributes chosen for this study are listed below:

1. Conversion Ratio
2. Multiplication Factor $\left(k_{eff}\right)$
3. Doppler Coefficient $\left(\frac{cents}{K}\right)$
4. Sodium Void Worth $(\$)$

Table 5 provides nominal values used in calculating the uncertainties listed in Table 6. Table 5 also lists the nominal values that were used in similar studies.

Table 5: Fast Reactor Nominal Values

		Nominal Value				
Key Core Attribute	**Units**	**Current Study**	**ABTR Report [2]**	**ABTR Study [13]**	**ANL Study [11]**	**Hoffman's Study [18]**
Multiplication Factor[b]	k_{eff} (pcm)	1.00638 (633.96)	--	--	1.0528 (5015.4)	--
Multiplication Factor[c]		0.99925 (-75.056)	--	0.99925 (-75.056)	--	--
Conversion Ratio[c]	--	0.7695	0.65	0.7695	0.25	0.75
Doppler Coefficient[b,e]	$\frac{cents}{K}$	-0.0788	-0.10	--	--	-0.10
Doppler Coefficient[c,e]		-0.0788	-0.10	--	(231 pcm)	-0.10
Sodium Void Worth[b]	$	2.0799	1.75	--	--	6.82
Sodium Void Worth[c]		1.8700	1.85	--	(1831 pcm)	7.12

Current Study:	**ABTR Study:**	**ANL Study:**	**Hoffman Study:**
[a] - 121.7 EFPD [b] - BOC [c] - EOC [d] - Peak Region: ICO_F [e] - Evaluated at (T_o=850K, T_1=950K)	- 250 MW_{th} Reactor - 121.7 EFPD -Na Cooled	-840 MW_{th} Reactor - 155 EFPD -Na Cooled	- 1000 MW_{th} Reactor - 232 EFPD -Na Cooled

As previously mentioned, REBUS was selected to model the ABTR core for a converted equilibrium to non-equilibrium scenario. The equilibrium model was provided by ANL [23]. For a non-equilibrium case, an explicit cycle-by-cycle operation for a reactor under a prescribed periodic or non-periodic fuel management program is utilized. In this scenario, the initial composition of the reactor core can be specified. In contrast, an equilibrium case operates under an infinite time-fixed fuel management program. External feed along with a reprocessing option can be utilized in this scenario [10]. For this study, the final core compositions were extracted from the equilibrium case and placed into a once through core model. These compositions were incorporated into a non-equilibrium model and burned over a 121.7 day irradiation period with inner-core, middle-core and outer-core batches of 12/15/12, respectively.

Following Eq. (3.4-4), the relative uncertainties for each attribute listed above were calculated and are documented in Table 6.

Table 6: Key Core Attribute Uncertainties

	Uncertainty (%)			
Key Core Attribute	**Current Study**	**ABTR Study [13]**	**ANL Study [11]**	**Palmiotti's Study [12]**
Multiplication Factor[b]	0.9808	--	--	--
Multiplication Factor[c]	0.9515	0.2180	1.66	1.0
Conversion Ratio[c]	2.1272	1.7147	--	5.0
Doppler Coefficient[b,e]	3.467	--	6.0	7.0 (total)
Doppler Coefficient[c,e]	13.987	--	--	
Sodium Void Worth[b]	11.3643	--	--	
Sodium Void Worth[c]	12.1598	--	23.4	

Current Study:
[a] - 121.7 EFPD
[b] - BOC
[c] - EOC
[d] - Peak Region: ICO_F
[e] - Evaluated at (T_o=850K, T_1=950K)

ABTR Study:
- 250 MW_{th} Reactor
- 121.7 EFPD
-Na Cooled

ANL Study:
-840 MW_{th} Reactor
- 155 EFPD
-Na Cooled

Palmiotti Study:
- 1000 MW_{th} Reactor
- 232 EFPD
-Na Cooled

The uncertainties that were created via this methodology are listed in the 'Current Study' column, whereas the adjacent columns to the right are similar studies conducted by other researchers listed here for comparison purposes [11],[12],[13]. Additional information regarding the reactor designs for each adjacent study can be found below Table 6. By running r_{post} forward model evaluations in REBUS, the uncertainty for a particular attribute was calculated by observing the difference between all perturbed cases with the nominal value. It can be seen that the uncertainties calculated for this study greatly resemble uncertainties that were documented for similar studies. Excluding the 'ABTR Study' listed in Table 6, the fast reactor designs, such as reactor power rating and burnup periods, did not exactly match the design for the current study, and therefore it was not an expectation to exactly match the uncertainties gathered from previous studies.

The target uncertainty for the multiplication factor was around 1% $\frac{\Delta k}{k}$ through comparison purposes of other studies. It was found that the k_{eff} uncertainty for this ABTR design came out to be 0.9808% $\frac{\Delta k}{k}$ and 0.9515% $\frac{\Delta k}{k}$ at BOC and EOC, respectively, using r_{post} forward model evaluations. Comparatively, k_{eff} uncertainty values for the other studies ranged from 0.2180% to 1.66%. Additionally, the fuel Doppler reactivity and sodium void worth were examined for this particular study. With liquid sodium as the primary coolant for the ABTR design, it was imperative to calculate the uncertainty for sodium void worth due to cross-section uncertainties since the sodium void worth is positive. At BOC, the Doppler coefficient uncertainty was found to be 3.467% which is similar to other data, whereas EOC uncertainty is 13.987%. Finally, the sodium void worth uncertainty was calculated at BOC/EOC to be 11.3643/12.1598%, respectively. The sodium void worth was calculated by evaluating the model with sodium coolant present in the core and once again by voiding any sodium coolant in the active fuel region of the core. Note that at hot-full power (HFP), the reactor fuel pellets experience radial and axial expansion which forces liquid sodium bond into a gas plenum which exists at the top of each fuel pin. Figure 15 presents a fuel assembly schematic and a cross-section cut representation of a fuel pin to show the fuel pellet and gas plenum locations in a fuel pin. Therefore, it was necessary to void the sodium coolant that exists in this region of each fuel assembly. Taking the difference between a sodium voided core with a non-voided core produced the sodium void worth. Eq. (3.4-4) was utilized to calculate the uncertainty in this attribute in the same manner as the other core attributes

shown in Table 6. This capability for quantifying uncertainties can be further used on core attributes such as peak discharge burnup, peak fast fluence, power peaking factor, peak linear power rate, etc.

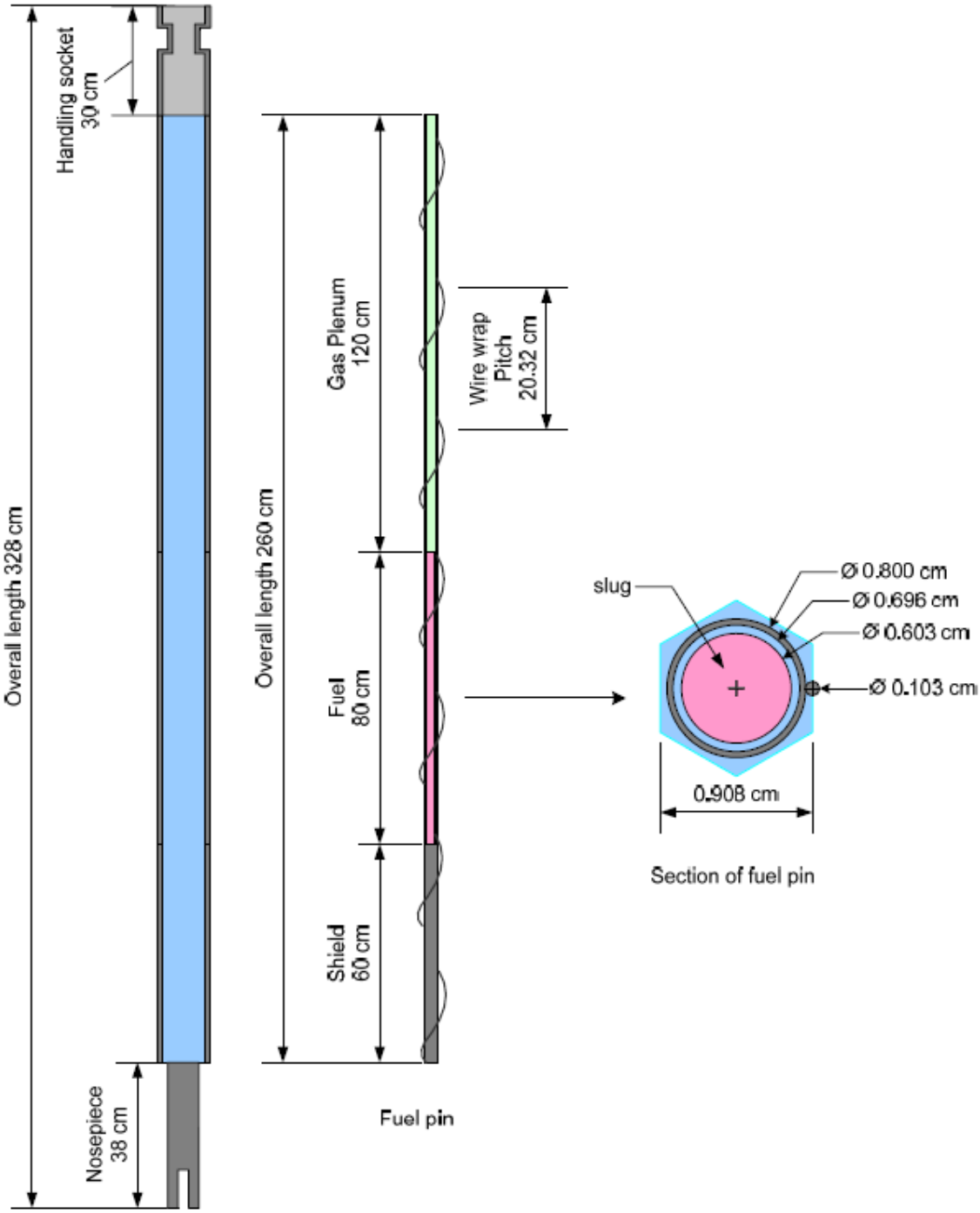

Figure 15: Fuel Assembly/Fuel Pin Schematic

Uncertainty data was also collected from the paper by G. Aliberti, et al., and is shown in Table 6 under 'ANL Study'. Aliberti used a sodium cooled fast reactor rated at 840 MW_{th} in his study. Similarly to the current study, a U-TRU-Zr metallic alloy fuel was utilized. Finally, with a conversion ratio of 0.25, the irradiation period lasted 155 days [11]. The uncertainty data that was calculated from the current study is comparable to that found in the ANL report.

G. Palmiotti performed an uncertainty analysis upon ANL's Sodium Fast Reactor (SFR) design. This uncertainty data can also be found in Table 6 under 'Palmiotti's Study.' There was a limited supply of uncertainty data that was calculated by Palmiotti; however, uncertainty values for the multiplication factor, conversion ration and reactivity coefficients are comparable to results from this study.

4.3.2 Key Cross-Section Uncertainty Quantification

As pointed out, this analysis can also help identify the key cross-sections contributing the most to the calculated uncertainties. A FORTRAN90 code was created to sort the first column vector of matrix $\mathbf{V}_{post}$ in descending order as per section 3.4.2 methodology. To accurately find which cross-sections were key in contributing to higher uncertainties, it was found that the elements of the uncertainty response matrix, $\mathbf{Y}_{post}$, shown in Eq. (3.3-2), needed to be set as absolute quantities instead of relative quantities. As described in section 3.4.2, the SVD is taken of the $\mathbf{Y}_{post}$ matrix. Further, the singular values, which correspond to individual cross-sections, are matched up with each row from $\mathbf{V}_{post}$. Since $\mathbf{Y}_{post}$ is in absolute quantities, the elements of $\mathbf{V}_{post}$ are now ordered on the absolute difference from the unperturbed case rather than relative percent. Thus,

higher level importance vectors from $\mathbf{V}_{post}$ which will contribute to higher attribute uncertainties are ordered from left to right. Therefore, the first column of $\mathbf{V}_{post}$, along with the corresponding singular values, were ordered in a descending fashion to find out which cross-sections contributed to higher attribute uncertainties.

Table 7 shown below provides a list of the top cross-sections that contributed to key attribute uncertainty shown in Table 5, followed by Table 8 which shows the 15-group energy ranges.

Table 7: Key Cross-Section Uncertainty

Isotope Label	Reaction Type	Energy Group	Uncertainty
Fe^{56}	(n,γ)	2	2.4696080E-01
Fe^{56}	(n,el)	1	1.1030110E-01
Cr^{52}	(n,el)	3	8.2986540E-02
Fe^{56}	(n,n')	1	2.8781800E-01
U^{236}	(n,γ)	3	1.1470010E-01
Pu^{240}	(n,γ)	1	6.1275610E-01

Table 8: 15-Group Energy Range

	Energy Range (eV)	
Energy Group	**Minimum Energy**	**Maximum Energy**
1	6.0654E+06	1.4191E+07
2	2.2313E+06	6.0654E+06
3	1.3533E+06	2.2313E+06
4	4.9788E+05	1.3533E+06
5	1.8316E+05	4.9788E+05
6	6.7381E+04	1.8316E+05
7	2.4788E+04	6.7381E+04
8	9.1190E+03	2.4788E+04
9	2.0347E+03	9.1190E+03
10	4.5401E+02	2.0347E+03
11	2.2604E+01	4.5401E+02
12	3.9939E+00	2.2604E+01
13	5.4052E-01	3.9939E+00
14	4.1400E-01	5.4052E-01
15	0	4.1400E-01

In Table 7, for each isotope the corresponding reaction type, energy group and relative cross-section uncertainty are provided. Reaction types are as follows: (n,γ), (n,el), (n,n') denote neutron-gamma, neutron-elastic scattering and neutron-inelastic scattering reactions, respectively. The uncertainties for each isotope/reaction are in units of relative standard deviation. Therefore, from this study, Fe^{56}, which has a neutron-gamma reaction in the second energy range shown in Table 7 is the highest contributor of uncertainty for key core attributes with an uncertainty of 24.69%. Fe^{56} is known for having a large elastic and inelastic scattering cross-section and is used for structural support. Further, Reference 11 documented that Fe^{56} (n,n') cross-section is the most significant structural/coolant material that contributes to higher core attribute uncertainties. Fissile isotopes such as U^{235}, Pu^{239} and Pu^{241} contain great potential to contribute uncertainty to key core attributes; however, these isotopes have been well-

studied by simulative and experimental methods. Table 9 shows the uncertainty data that was collected for these fissile isotopes.

Table 9: Fissile Isotope Cross-Section Uncertainty

Isotope Label	Reaction Type	Energy Group	Uncertainty
U^{235}	(n,γ)	2	8.1283430E-02
U^{235}	(n,f)	3	7.8423090E-03
Pu^{239}	(n,γ)	4	1.2353180E-02
Pu^{239}	(n,f)	2	8.5398370E-02
Pu^{241}	(n,γ)	1	8.3700860E-03
Pu^{241}	(n,f)	1	3.5999780E-02

For these selected isotopes, the neutron-gamma and neutron-fission reactions were chosen. It can be seen in Table 9 that the uncertainties found for these fissile isotopes are smaller than the uncertainties presented in Table 7. These isotopes may have been very sensitive in this system; however, due to lower uncertainties than many other isotopes they were not key contributors to higher attribute uncertainty.

5 Conclusions

This work presents a new UQ algorithm that places a premium on minimizing the computational overhead, and ease of implementation. The approach exploits the rank reduction that often results from the continuous dimensionality reduction that is characteristic of most computational sequences. Our concern is mainly with more routine design calculations that must be performed very frequently and that requires uncertainty estimates for a wide range of performance attributes to help in system design and optimization. By use of the forward model method, this study was able to pinpoint particular cross-sections that highly contributed to key core attribute uncertainty. Also, following a ESM methodology, the efficiency in uncertainty quantification techniques were increased by realizing that model dimensionality reduction was present in this study.

Of greater importance lies within the uncertainty values calculated for chosen key core attributes. These attributes were chosen due to their effect upon ABTR performance, safety and design optimization. It was a goal of this study to place a dollar value on the uncertainties found for each key core attribute. Not only would realistic uncertainty estimates allow reactor design specialists to 'fine tune' design margins, power utilities would be able to calculate a net loss of revenue due to such uncertainties. Hopefully, the information gathered from the UQ development in this paper will encourage the nuclear industry to investigate how these uncertainties influence power and safety margins in their corresponding plants. Overall, these results provide some knowledge behind the importance in uncertainty quantification on the microscopic data level, i.e. cross-section data.

6 Future Work

Future work will focus on employing the developed methodology to characterize uncertainties in various core attributes judged to have an important impact on the overall reactor economy, e.g. shutdown heat, and discharged fuel heat load and radio-toxicity, etc. The cross-sections impacting key performance metrics uncertainties can be identified as demonstrated in this study. Further, an adaptive simulation device can be used to design the optimum experiment to reduce uncertainties of the identified key cross-section, e.g. optimize the design of (Zero Power Physics Reactor) ZPPR benchmark facility used in support of the sodium-cooled fast reactors experiments. Finally, a cost of margin can be placed upon the uncertainties calculated in this study for each key core attribute. Thus, analyst can evaluate the cost-benefit of reducing these uncertainties by experimentation and/or improve the accuracy of modeling systems.

References

1. A.E. Dubberley, K. Yoshida, C.E. Boarman, and T. Wu, "SuperPRISM Oxide and Metal Fuel Core Designs," Proceedings of ICONE 8, 8th International Conference on Nuclear Engineering, 2000.

2. Y.I. Chang, P.J. Finch, and C. Grandy, "ABTR Preconceptual Design Report," Argonne National Laboratories, Nuclear Engineering Division, 2006.

3. H.S. Abdel-Khalik, P.J. Turinsky, and M.A. Jessee, "Efficient Subspace Methods-Based Algorithms for Performing Sensitivity, Uncertainty, and Adaptive Simulation of Large-Scale Computational Models," Accepted for publication in Nucl. Sci. & Eng., 2007.

4. M.A. Jessee, H.S. Abdel-Khalik, and P.J. Turinsky, "Evaluation of BWR Core Attributes Uncertainties due to Multigroup Cross-Section Uncertainties," Proceedings from Mathematical and Computation Topical Meeting, Monterey, CA, 2007.

5. Argonne National Laboratory, MC^2-2: Code System for Calculating Fast Neutron Spectra and Multigroup Cross-Sections, PSR-350, MC^2-2, 2000.

6. D. Rochman, et al., "Preliminary Cross Section and v-bar Covariances for WPEC Subgroup 26," National Nuclear Data Center. Brookhaven National Laboratory. BNL-77407-2007-IR, 2007.

7. J. Duderstadt, and L. Hamilton, Nuclear Reactor Analysis, Hoboken, NJ. John Wiley & Sons, Inc., 1976.

8. T.E. Stover, H.S. Abdel-Khalik, and P.J. Turinsky, "Quantification of Back-End Fuel Cycle Metrics Uncertainties," Trans. of the Am. Nucl. Soc., Summer Mtg., **96**, Boston, 2007.

9. H.S. Abdel-Khalik, "Adaptive Core Simulation," Ph.D. Dissertation, North Carolina State University, 2004.

10. Argonne National Laboratory, REBUS-3/VARIANT8.0: Code System for Analysis of Fast Reactor Fuel Cycles, CCC-653, REBUS-3, Variant 8.0, 2001.

11. G. Aliberti, et al., "Nuclear Data Sensitivity, Uncertainty and Target Accuracy Assessment for Future Nuclear Systems," Annals of Nuclear Energy, **33**, 2006.

12. G. Palmiotti, "Reactor Core Advanced Simulation," Power Point Pres., Private Communication.

13. T.E. Stover, "Quantification of Back-End Fuel Cycle Metrics Uncertainties Due to Cross Sections," M.S. Thesis, North Carolina State University, 2007.

14. Yigal Ronen, Uncertainty Analysis, Boca Raton, FL. CRC Press Inc., 1988.

15. Yigal Ronen, Handbook of Nuclear Reactors Calculations, Vol III, Boca Raton, FL. CRC Press Inc., 1986.

16. G.D. Wyss, and K.H. Jorgensen. "A User's Guide to LHS: Sandia's Latin Hypercube Sampling Software," Sandia National Laboratory, 1998.

17. Workshop on Simulation and Modeling for Advanced Nuclear Energy Systems, co-sponsored by Office of NE, Office of ACCR, and U.S. DOE, Washington, D.C., 2006 [htt://www-fp.mcs.anl.gov/anes/SMANES/gnep06-final.pdf].

18. E.A.Hoffman, W.S. Yang, and R.N. Hill, "Preliminary Core Design Studies for the Advanced Burner Reactor Over a Wide Range of Conversion Ratios," Argonne National Laboratory, Argonne, IL, 2006.

19. C.D. Meyer, Matrix Analysis and Applied Linear Algebra, Philadelphia, PA. SIAM, 2000.

20. M. Iqbal, Private Communication, 2007.

21. R. A. Waller, Statistics: An Introduction to Numerical Reasoning, San Francisco, CA. 1979.

22. R. E. Walpole, Introduction to Statistics, New York, NY. Macmillan Publishing Co Inc., 1982.

23. Won Sik Yank, Private Communication, 2007.

Appendices

1 Neutron Capture/Absorption Cross-Section Figures

The following section presents the neutron capture or absorption cross-section figures from the ENDF/B 6.1 libraries for the isotopes that make up core structural materials and the coolant region. These isotopes include: ^{10}B, ^{12}C, ^{23}Na, ^{52}Cr, ^{55}Mn, ^{56}Fe, ^{58}Ni and ^{100}Mo. The reflector, shield and barrel region of the core are structurally created of stainless steel, which is a alloy containing Fe, C, Cr and a small fraction of other metals. Additionally, this reactor core is cooled by liquid sodium and therefore the total absorption cross-section is shown for ^{23}Na. At higher energies, such as the fast neutron spectrum seen in this study, the neutron capture and/or absorption cross-sections for these isotopes are negligible as can be seen in the following figures. It is due to this reason that the reactions created by these isotopes were removed from Figures 4.2-2 and 4.2-3.

Isotope: B-10

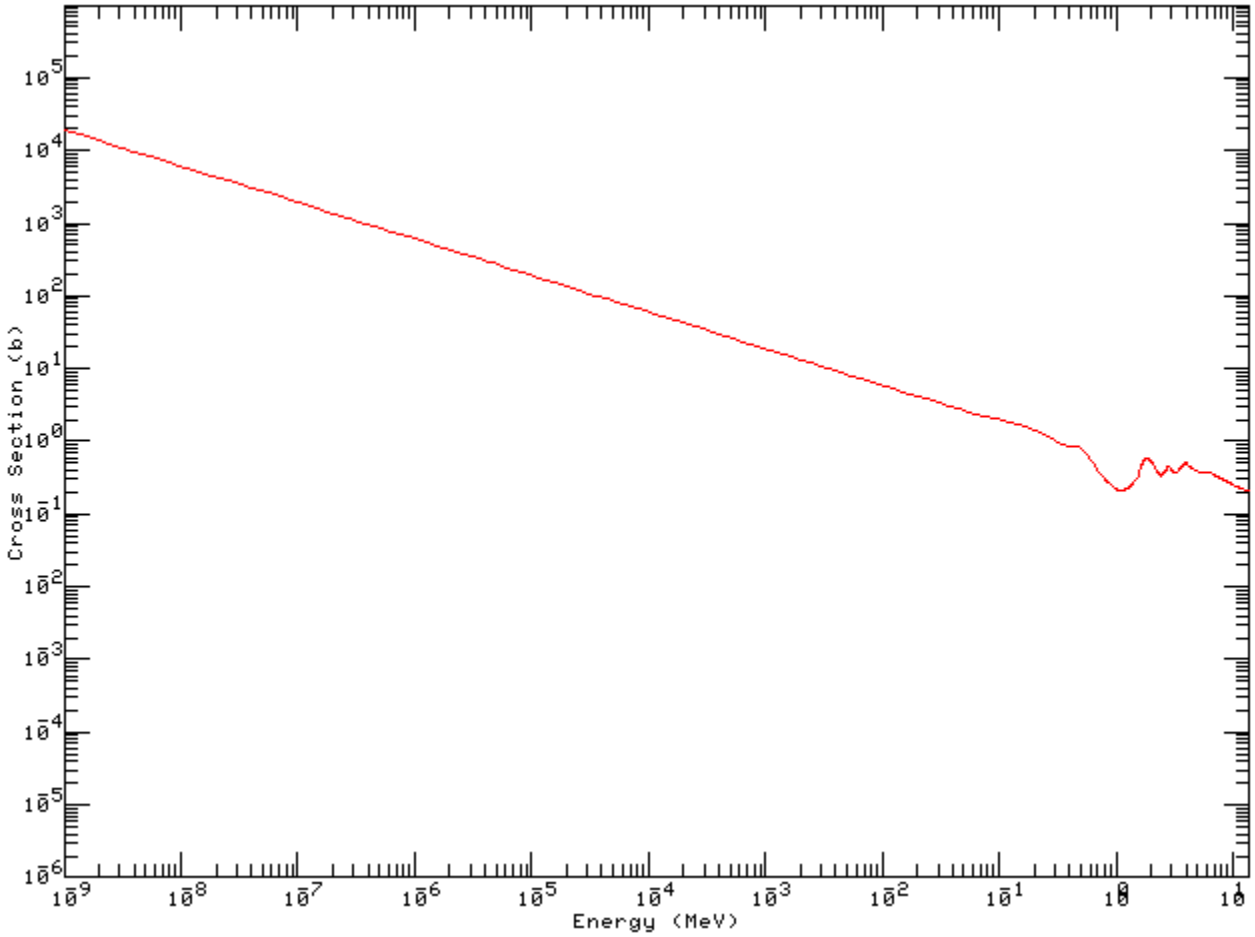

Figure 16: B-10 Total Absorption Cross-Section

Isotope: C-12

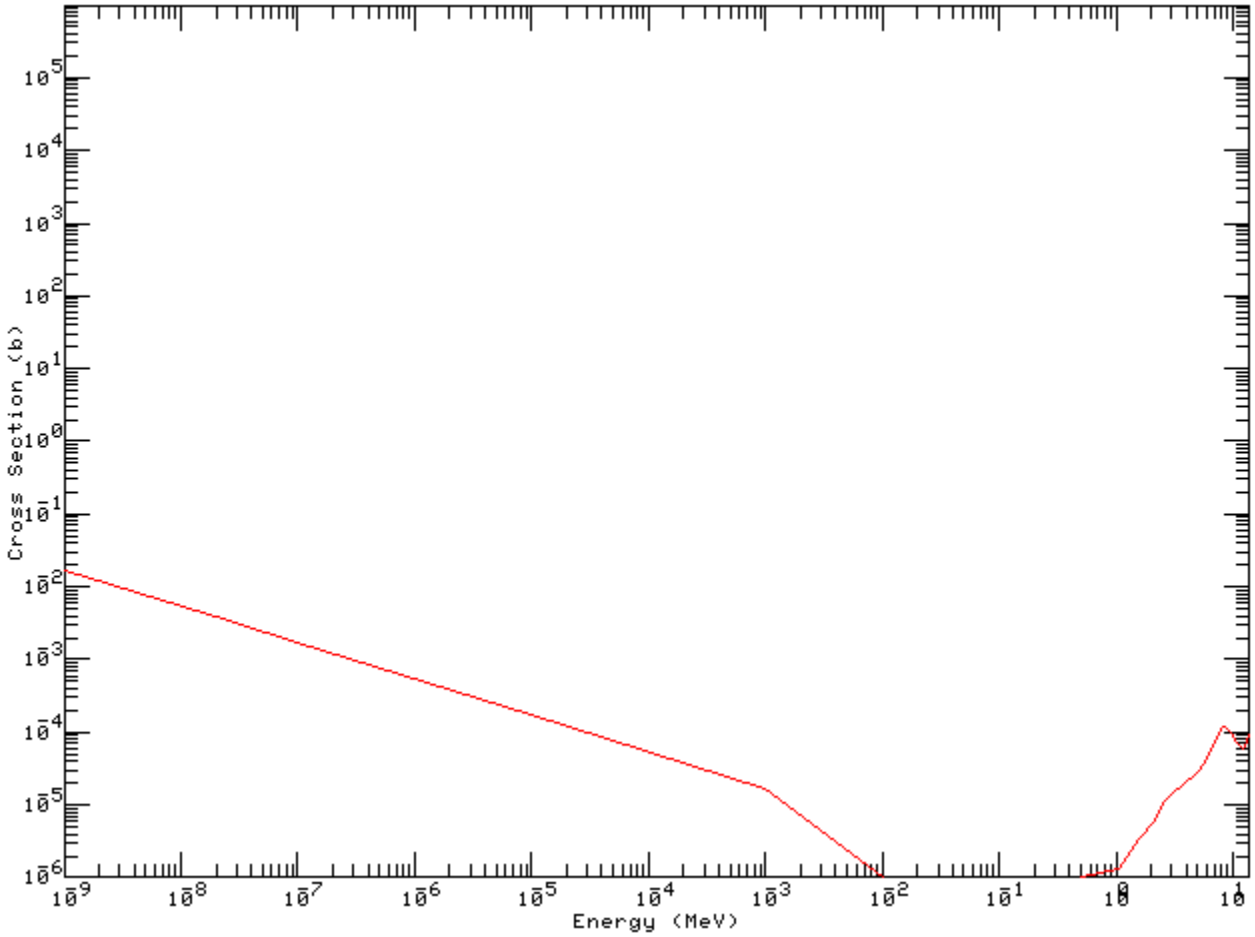

Figure 17: C-12 Radiative Capture Cross-Section

Isotope: Na-23

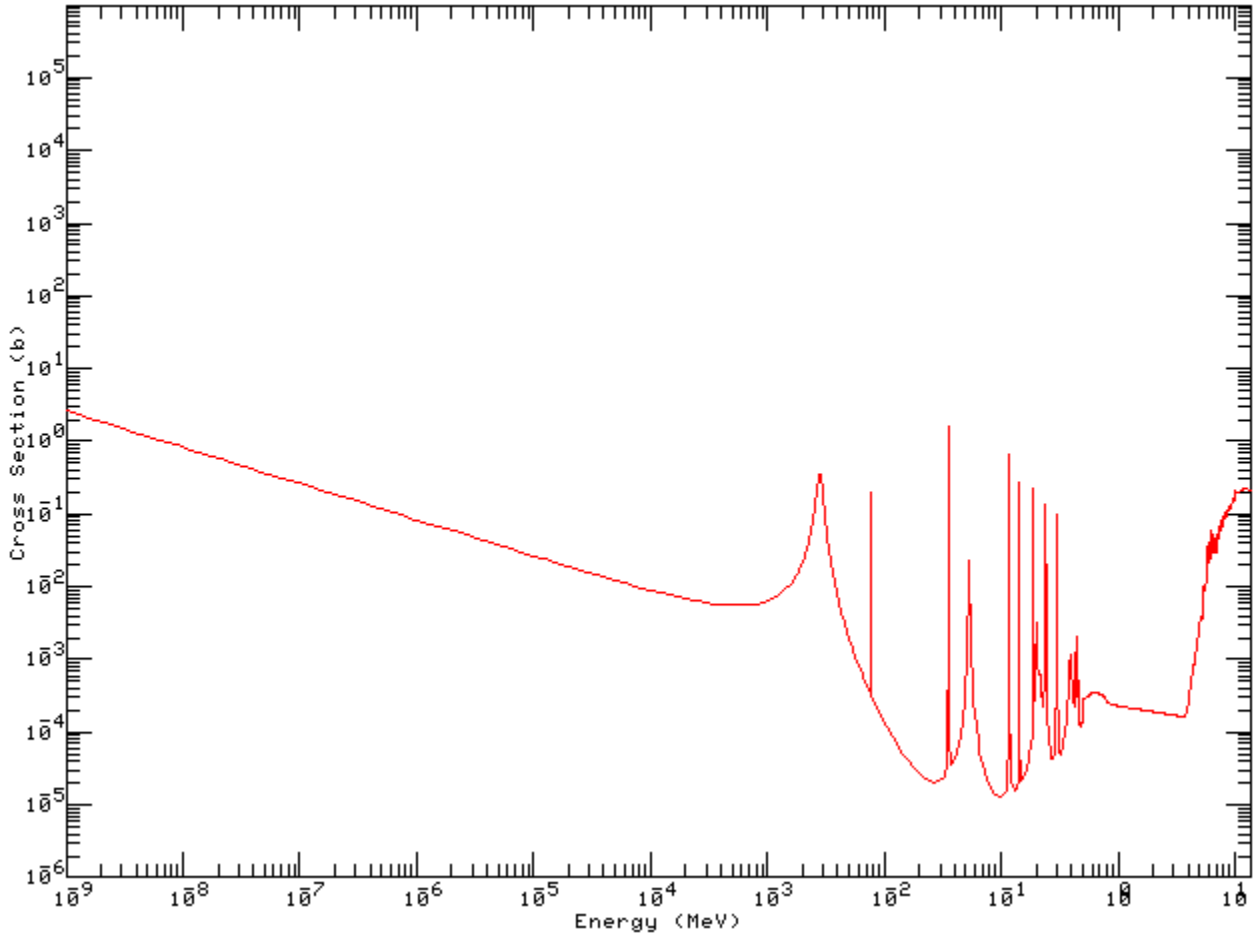

Figure 18: Na-23 Total Absorption Cross-Section

Isotope: Cr-52

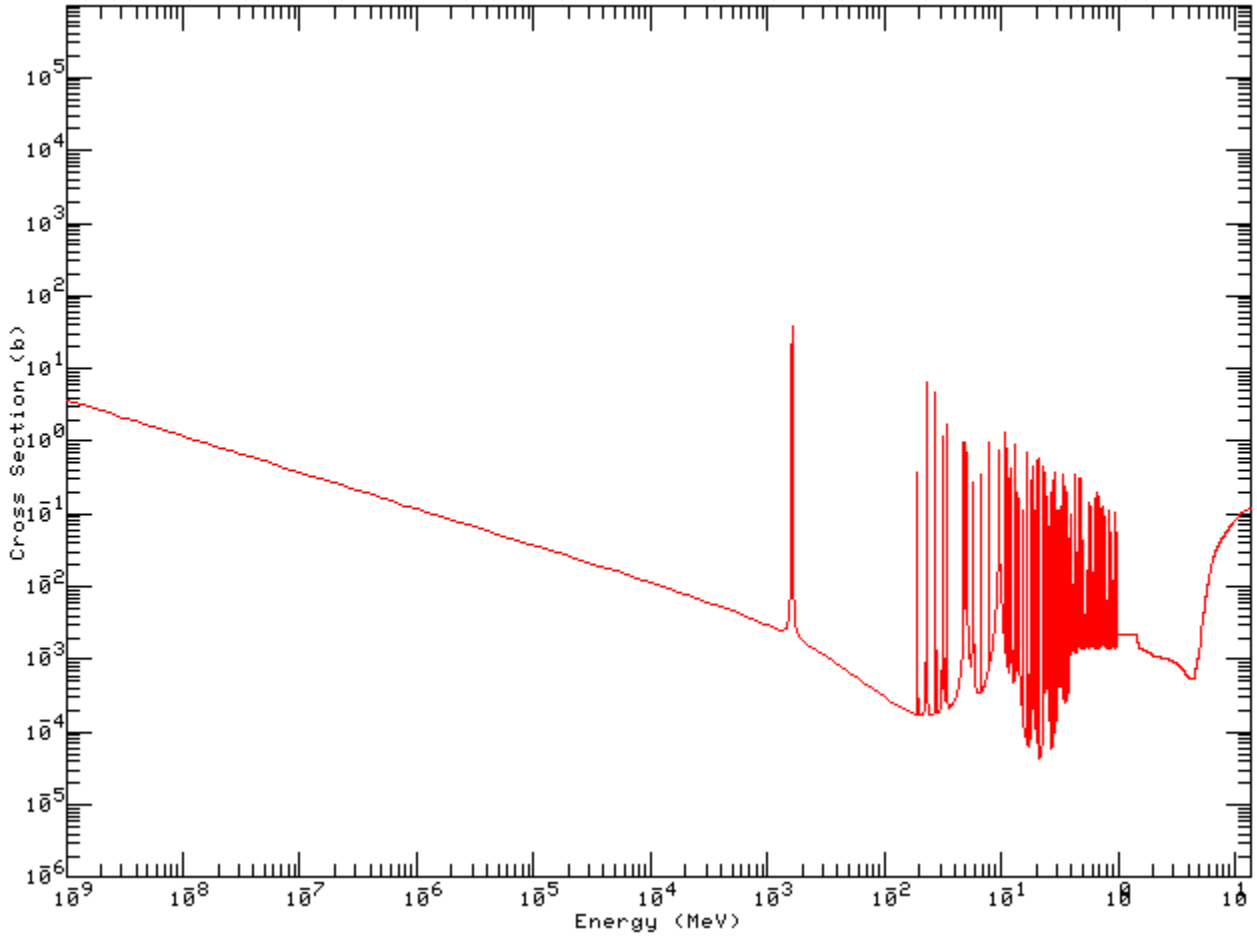

Figure 19: Cr-52 Total Absorption Cross-Section

Isotope: Mn-55

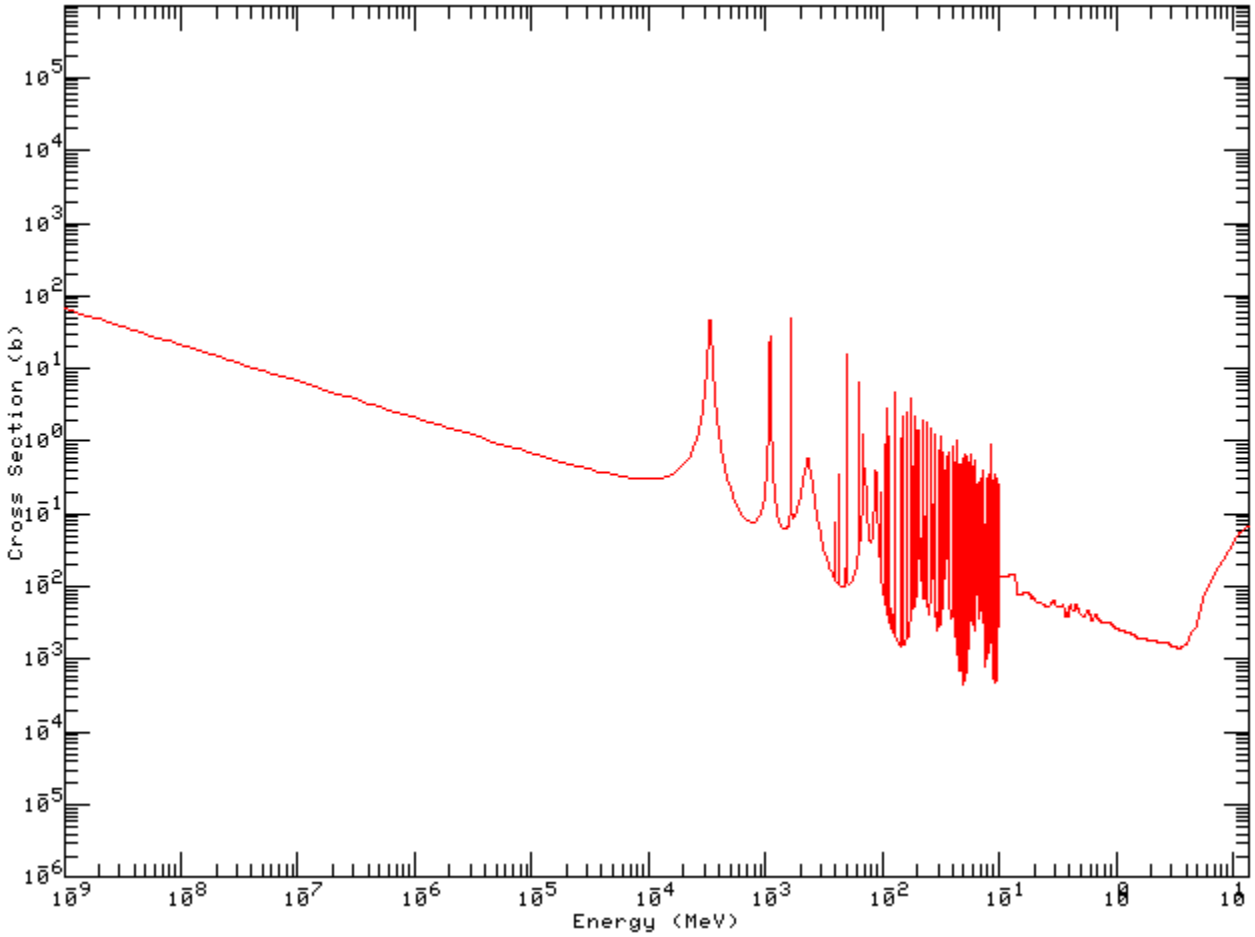

Figure 20: Mn-55 Total Absorption Cross-Section

Isotope: Fe-56

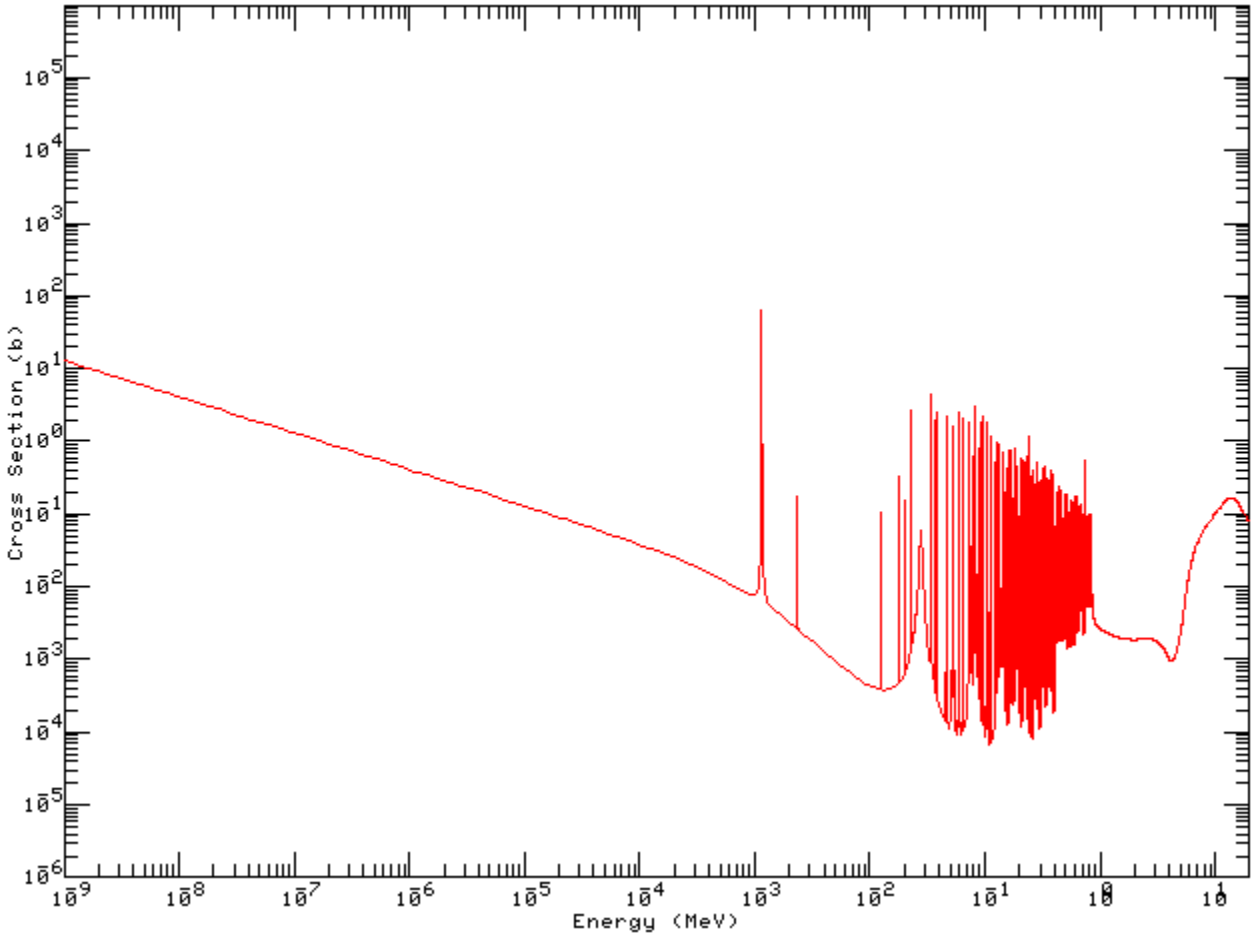

Figure 21: Fe-56 Total Absorption Cross-Section

Isotope: Ni-58

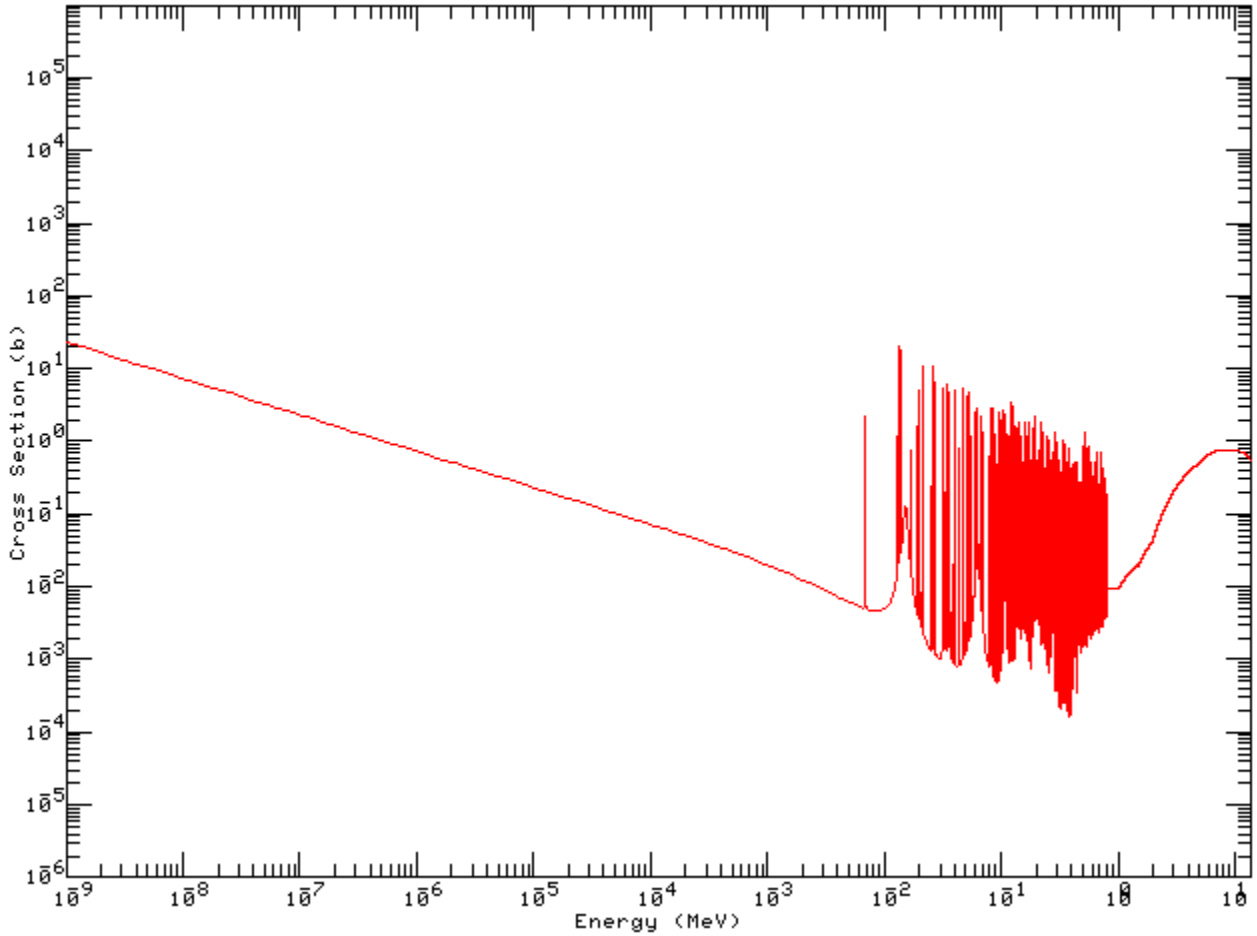

Figure 22: Ni-58 Total Absorption Cross-Section

Isotope: Mo-100

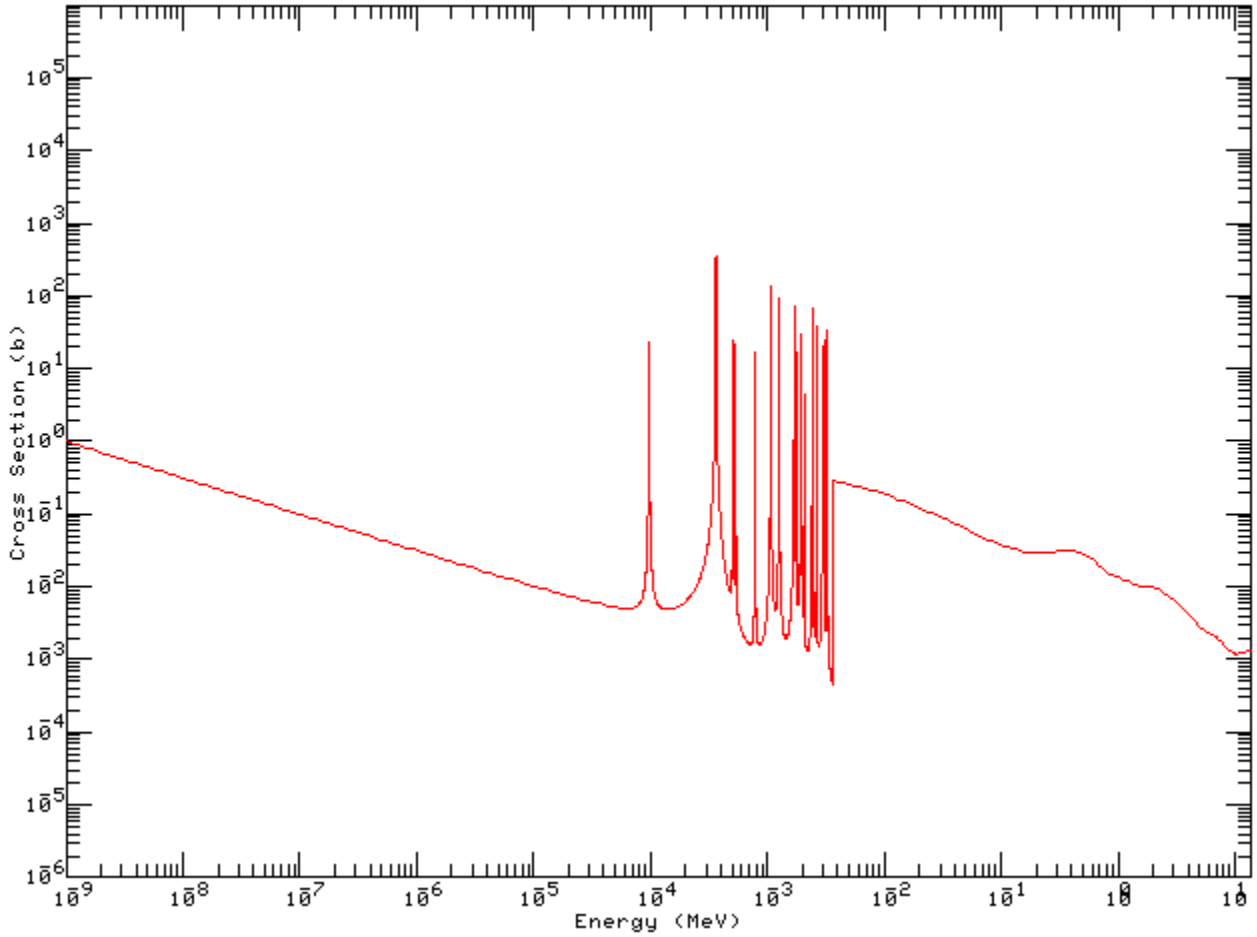

Figure 23: Mo-100 Total Absorption Cross-Section

2 Neutron Flux Spectrum Figures

The following figures present the neutron flux spectrums over the 15 energy groups for the inner-core, middle-core and outer-core regions, respectively.

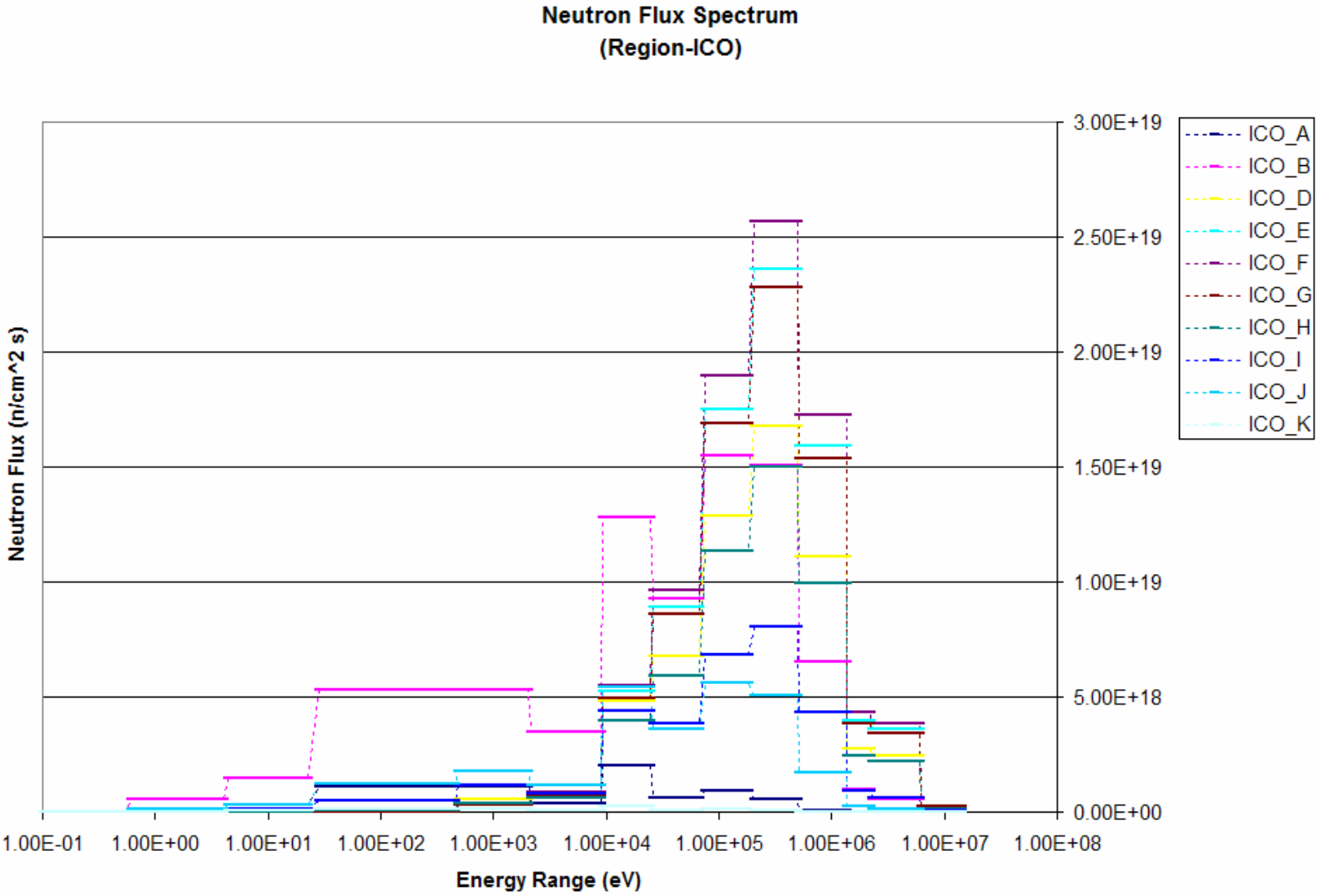

Figure 24: Inner-Core Neutron Flux Spectrum

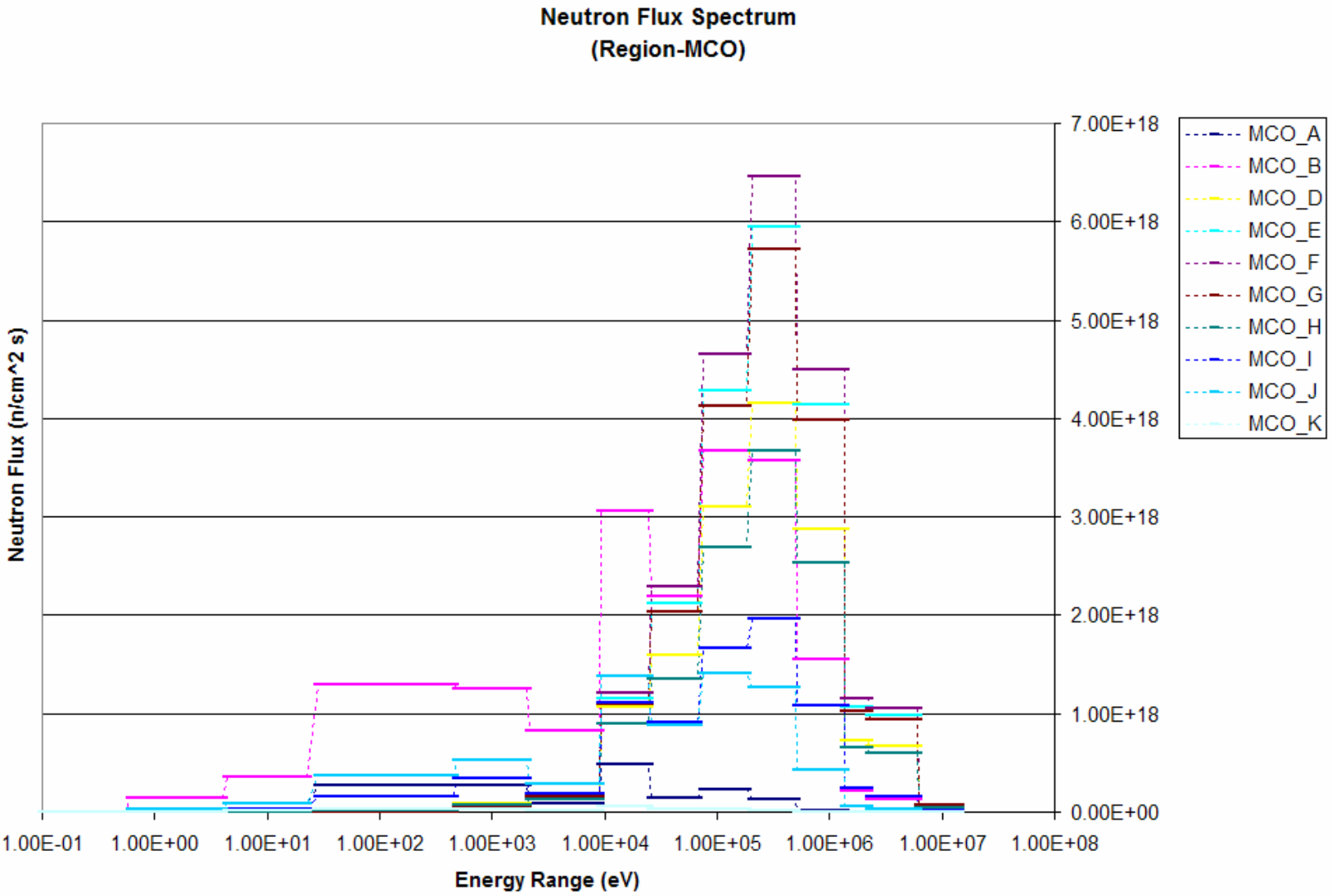

Figure 25: Middle-Core Neutron Flux Spectrum

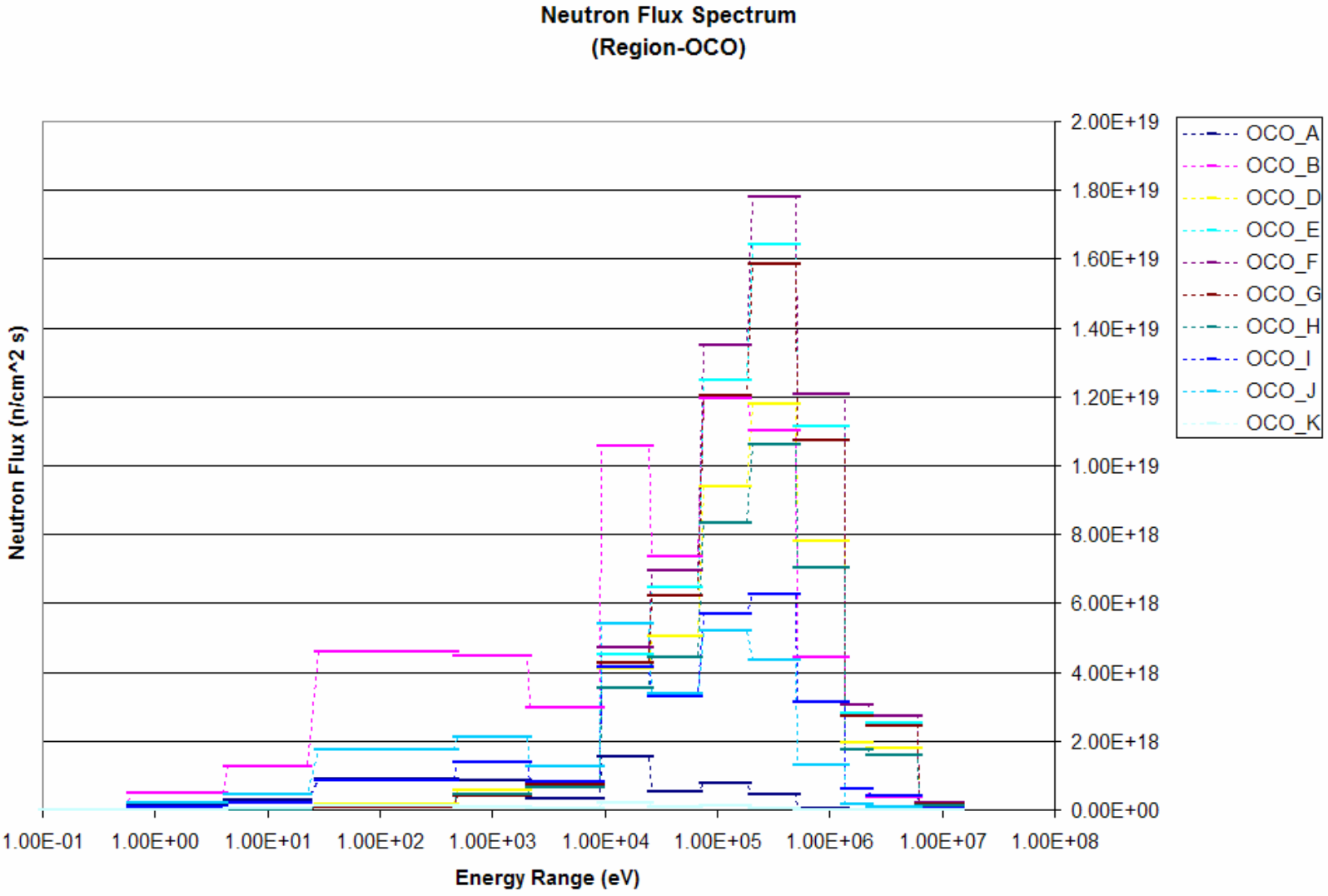

Figure 26: Outer-Core Neutron Flux Spectrum